

**AD-A274 063**



**Quarterly Technical Report**

**Solid State Research**

**S** **DTIC**  
**ELECTE**  
**DEC 22 1993**  
**A**

**1993:2**

**Lincoln Laboratory**  
**MASSACHUSETTS INSTITUTE OF TECHNOLOGY**  
**LEXINGTON, MASSACHUSETTS**



**Prepared for the Department of the Air Force under Contract F19628-90-C-0002.**

**Approved for public release; distribution is unlimited.**

**93-30831**



**93 12 21 171**

This report is based on studies performed at Lincoln Laboratory, a center for research operated by Massachusetts Institute of Technology. The work was sponsored by the Department of the Air Force under Contract F19628-90-C-8002.

This report may be reproduced to satisfy needs of U.S. Government agencies.

The ESC Public Affairs Office has reviewed this report, and it is releasable to the National Technical Information Service, where it will be available to the general public, including foreign nationals.

This technical report has been reviewed and is approved for publication.

FOR THE COMMANDER



Gary Tutungian  
Administrative Contracting Officer  
Directorate of Contracted Support Management

Non-Lincoln Recipients

PLEASE DO NOT RETURN

Permission is given to destroy this document  
when it is no longer needed.

**MASSACHUSETTS INSTITUTE OF TECHNOLOGY  
LINCOLN LABORATORY**

**SOLID STATE RESEARCH**

**QUARTERLY TECHNICAL REPORT**

**1 FEBRUARY — 30 APRIL 1993**

**ISSUED 30 SEPTEMBER 1993**

**Approved for public release; distribution is unlimited.**

**LEXINGTON**

**MASSACHUSETTS**

## ABSTRACT

This report covers in detail the research work of the Solid State Division at Lincoln Laboratory for the period 1 February through 30 April 1993. The topics covered are Electrooptical Devices, Quantum Electronics, Materials Research, Submicrometer Technology, High Speed Electronics, Microelectronics, and Analog Device Technology. Funding is provided primarily by the Air Force, with additional support provided by the Army, DARPA, Navy, SDIO, and NASA.

Accession For		
NTIS	CRA&I	<input checked="" type="checkbox"/>
DTIC	TAB	<input type="checkbox"/>
Unannounced		<input type="checkbox"/>
Justification .....		
By .....		
Distribution /		
Availability Codes		
Dist	Avail and/or Special	
A-1		

[DTIC QUALITY INSPECTED 3]

## TABLE OF CONTENTS

Abstract	iii
List of Illustrations	vii
List of Tables	ix
Introduction	xi
Reports on Solid State Research	xiii
Organization	xxi
 1. ELECTROOPTICAL DEVICES	 1
1.1 Monolithic Optoelectronic Transistor	1
 2. QUANTUM ELECTRONICS	 5
2.1 Holmium Laser Pumped by 1.9- $\mu$ m Diode Laser	5
 3. MATERIALS RESEARCH	 9
3.1 MBE Growth and Characterization of PbTe <sub>0.8</sub> Se <sub>0.2</sub> Films	9
 4. SUBMICROMETER TECHNOLOGY	 13
4.1 Acid-Catalyzed Single-Layer Resist for 193-nm Lithography	13
4.2 Diamond Field-Emission Cathode Technology	16
 5. HIGH SPEED ELECTRONICS	 23
5.1 Photonic-Crystal Planar Antennas	23
 6. MICROELECTRONICS	 27
6.1 Method for Measuring Quantum Efficiency of CCD Imagers	27
 7. ANALOG DEVICE TECHNOLOGY	 31
7.1 Cylindrical Magnetron Deposition of High-Quality High-Temperature Superconductive Thin Films	31
7.2 Tunnel-Diode Shift Register Using Tunnel-Diode Coupling	35

## LIST OF ILLUSTRATIONS

Figure No.	Page
1-1 (a) Circuit of simplest version of monolithic optoelectronic transistor (MOET). (b) Current-voltage (I-V) characteristic of resonant-tunneling diode (RTD). The operating points just before and just after the field-effect transistor (FET) turns on are indicated by points A and B, respectively. The dashed arrows show the abrupt changes in operating point that occur at the switching points of the MOET device. (c) Drain-source I-V characteristics of the FET just before and just after it turns on. The I-V characteristic of the illuminated modulator is included as a nonlinear load line. In its low-reflectivity state, the modulator is highly absorbing and produces much more photocurrent than in the high-reflectivity state. (d) Expected optical transfer characteristic of the MOET.	2
1-2 Cross section showing structure of MOET after circuit fabrication is complete. The only metallization connection not shown is from the <i>p</i> side of the detector to the gate of the FET. Also not shown is the silicon nitride layer.	3
1-3 Measured optical transfer characteristic of MOET at modulator illumination levels giving on-state output power of 140 $\mu$ W for (a) $V_{gg} = 5.8$ V and (b) $V_{gg} = 5.4$ V.	3
2-1 Ho laser output vs absorbed pump power. The line fit is to the last four points only.	6
2-2 Ho laser output vs crystal temperature.	6
3-1 [444] x-ray diffraction lines for $\text{PbTe}_{0.8}\text{Se}_{0.2}$ film grown by molecular beam epitaxy (MBE).	10
3-2 Optical micrographs of (a) cleaved cross section of $\text{PbTe}_{0.8}\text{Se}_{0.2}$ MBE-grown film on (111) $\text{Ba}_2\text{F}$ substrate and (b) as-grown surface of $\text{PbTe}_{0.8}\text{Se}_{0.2}$ film.	11
4-1 Absorption coefficient at 194 nm of poly(MMA- <i>co</i> -tBMA- <i>co</i> -MAA) terpolymer as function of photoacid generator (PAG) loading. The PAG was bis( <i>t</i> -butylphenyl) iodonium triflate. Also shown is the sensitivity of the resist vs PAG loading, after a 130°C, 1-min post-exposure bake.	14
4-2 Contrast curve for poly(MMA- <i>co</i> -tBMA- <i>co</i> -MAA) with 1% bis( <i>t</i> -butylphenyl) iodonium triflate PAG, developed in 0.01-N TMAH after a 130°C, 1-min post-exposure bake.	14
4-3 Resist profiles for sample using 1% bis( <i>t</i> -butylphenyl) iodonium triflate PAG. The process conditions were the same as for Figure 4-2. The exposures were carried out at 193 nm on a prototype stepper with 0.5 numerical aperture. The scanning electron micrographs illustrate features (a) 0.3, (b) 0.35, (c) 0.4, and (d) 0.5 $\mu\text{m}$ .	15

## LIST OF ILLUSTRATIONS (Continued)

Figure No.	Page
4-4 Resist profile for sample whose composition and process conditions were the same as for Figure 4-3, but in this case a chromeless phase-shifting mask was used. The line-width is $0.1\ \mu\text{m}$ and the resist thickness $0.5\ \mu\text{m}$ .	16
4-5 Measured emission characteristics of (100)- and (110)-oriented films fabricated by boron-doped homoepitaxy on single-crystal diamond substrates. The current vs voltage characteristic is strongly dependent on the crystal orientation of the substrate.	18
4-6 Scanning electron micrographs of (a) array of posts etched into a (100)-oriented, single-crystal diamond substrate and (b) detail of one such diamond post.	19
4-7 Comparison of the emission characteristics of planar, (100)-oriented, single-crystal diamond film and post array etched into the same film.	20
5-1 Schematic diagram of bow-tie antenna mounted on three-dimensional photonic-crystal substrate. Also shown is the experimental setup used to measure the radiation patterns at 13.2 GHz.	24
5-2 (a) Radiation pattern at 13.2 GHz measured over $360^\circ$ in the E-plane for bow-tie antenna on photonic-crystal substrate (radial scale linear in power). (b) Radiation pattern measured for same bow-tie antenna as in (a) but on uniform-dielectric substrate.	24
6-1 (a) Charge-coupled device with $3 \times 3$ array of uniformly illuminated pixels. (b) Square-wave-modulated photon flux incident on the device. (c) Amplitude $Q(t)$ of output charge packets as function of time in response to the modulated photon flux.	28
6-2 Experimental configuration for quantum efficiency measurement technique.	29
6-3 Comparison of quantum efficiency measured using normal imaging and clocked photodiode techniques.	30
7-1 Cross section of cylindrical magnetron. The magnetic field lines superposed on half of the figure were calculated using commercially available software [9].	32
7-2 $2\theta$ diffraction pattern of 800-nm YBCO thin film.	34
7-3 Surface resistance as function of peak RF magnetic field produced by RF currents circulating in center conductor of stripline resonator.	34
7-4 Basic resonant-tunneling diode (RTD) latch circuit.	35

## LIST OF ILLUSTRATIONS (Continued)

Figure No.		Page
7-5	Load-line graphical technique for analyzing behavior of RTD latch. The current-voltage (I-V) curves are solid and the load lines dashed. (a) Curves for a value of $I_{inj}$ for which there are three equilibrium states, two stable and one unstable. (b) Curves for the extreme values of $I_{inj}$ beyond which only one stable equilibrium state remains. In (b) the upper dashed curve shows the maximum current $I_{snk}$ that the latch can sink while in its low state before it switches to the high state, and the lower dashed curve shows the maximum current $I_{src}$ that the latch can source while in its high state.	36
7-6	Schematic of tunnel-diode shift register proposed by Aleksander and Scarr [13].	37
7-7	Sequence of I-V curves (solid) with load lines (dashed). The sequence shows how the state of the latch evolves as the clock voltage, having been pulsed low, returns to its normal high voltage. The upper curves are for the case of no current injected into the latch, and the lower curves for current injected into the latch. The clock voltages are low, in the critical interval, and high for (a), (b), and (c), respectively.	38
7-8	Oscilloscope traces during operation of prototype shift register using discrete components. The upper trace shows the input signal applied to the first latch, and the bottom two traces show the voltages at the input/output nodes of the first two latches. The timing of the two clock phases can be seen from the lowest output levels of the latch signals.	39
7-9	Scanning electron micrograph of first monolithic implementation of RTD-coupled shift register. The two vertical bus bars on the left are the two clock phases. The large bus bar on the right is ground. Pairs of RTDs share each well. In the wells on the left, the large RTD is the load device, and the small one the Schottky-contacted coupling device. The large RTDs in the wells on the right are the active devices for the two latches that constitute one stage of the shift register.	40

## LIST OF TABLES

Table No.		Page
3-1	Physical Properties of MBE-Grown $\text{PbTe}_{0.8}\text{Se}_{0.2}$ Films	12
7-1	Parameters for Cylindrical Magnetron Film Deposition	33



## INTRODUCTION

### 1. ELECTROOPTICAL DEVICES

A new optical switching and logic device, the monolithic optoelectronic transistor, has been demonstrated. The current devices switch at an optical input power of  $12.5 \mu\text{W}$  and have a large-signal optical gain  $> 10$ .

### 2. QUANTUM ELECTRONICS

The first direct diode pumping of the  $^5I_7 - ^5I_8$  transition in Ho:YAG has been achieved, with lasing at  $2.12 \mu\text{m}$  using a  $1.91\text{-}\mu\text{m}$  GaInAsSb diode laser pump. The slope efficiency is 45% for absorbed power.

### 3. MATERIALS RESEARCH

Films of  $\text{PbTe}_{0.8}\text{Se}_{0.2}$  have been grown by molecular beam epitaxy on  $18 \times 18 \times 1\text{-mm}$ , [111]-oriented, cleaved, single-crystal  $\text{BaF}_2$  substrates for evaluation as one of the components in a thermoelectric superlattice. Record high Seebeck coefficients or thermopowers of  $390 \mu\text{V/K}$  at 300 K and record low electron carrier concentrations of  $1.1 \times 10^{16} \text{ cm}^{-3}$  at 77 K were obtained.

### 4. SUBMICROMETER TECHNOLOGY

A positive-tone single-layer resist for use with 193-nm radiation has been developed with a demonstrated sensitivity of  $10 \text{ mJ/cm}^2$  and a resolution of  $0.1 \mu\text{m}$ . The resist contains a terpolymer of methyl methacrylate, methacrylic acid, and *t*-butyl methacrylate, along with a photoacid generator.

The electron emission properties of diamond films have been studied for possible application as cathodes for flat-panel displays. Stable, robust, low-field operation has been demonstrated.

### 5. HIGH SPEED ELECTRONICS

A coplanar metallic bow-tie antenna has been fabricated on a photonic-crystal substrate and tested at microwave frequencies. This antenna has demonstrated a radiation efficiency of nearly 100% into free space above the substrate.

### 6. MICROELECTRONICS

A new method of measuring quantum efficiency of CCD imagers is described, which makes use of the superior performance against noise of synchronous detection while operating the CCD with normal clocking waveforms. The results show excellent agreement with a standard method in wide use.

## **7. ANALOG DEVICE TECHNOLOGY**

A cylindrical magnetron sputtering source has been developed that is specially designed for the deposition of high- $T_c$  superconductors. Films of  $\text{YBa}_2\text{Cu}_3\text{O}_{7-\delta}$  deposited using this source have the best high-power RF properties yet reported.

A new circuit for realizing a very high speed digital shift register has been designed and fabricated, using resonant-tunneling diodes (RTDs) not only in the latches but also in the interstage coupling circuits. The coupling RTDs provide current flow only when needed to transfer data, thereby extending the operating margins and allowing for fan-out.

## REPORTS ON SOLID STATE RESEARCH

1 FEBRUARY THROUGH 30 APRIL 1993

### PUBLICATIONS

- |   |  |  |
|---|--|--|
| Methacrylate Terpolymer Approach<br>in the Design of a Family of Chemically<br>Amplified Positive Resists                                     | R. D. Allen*<br>G. M. Wallraff*<br>W. D. Hinsberg*<br>L. L. Simpson*<br>R. R. Kunz | <i>Polym. Mater. Sci. Eng.</i><br><b>66</b> , 251 (1992) |
| Coherent Detection with a GaAs/AlGaAs<br>Multiple Quantum Well Structure  | E. R. Brown<br>K. A. McIntosh<br>F. W. Smith<br>M. J. Manfra                       | <i>Appl. Phys. Lett.</i> <b>62</b> , 1513<br>(1993)      |
| Coherent Millimeter-Wave<br>Generation by Heterodyne<br>Conversion in Low-Temperature-<br>Grown GaAs Photoconductors                          | E. R. Brown<br>F. W. Smith<br>K. A. McIntosh                                       | <i>J. Appl. Phys.</i> <b>73</b> , 1480<br>(1993)         |
| Frequency Dispersion of<br>Transconductance and Output<br>Resistance in GaAs MESFETs with<br>Low-Temperature-Grown GaAs<br>Passivation Layers | C. L. Chen<br>F. W. Smith<br>L. J. Mahoney<br>M. J. Manfra<br>A. R. Calawa         | <i>Electron. Lett.</i> <b>29</b> , 499 (1993)            |
| Vertical Gradient-Freeze Growth of<br>Aluminate Crystals  | R. E. Fahey<br>A. J. Strauss<br>A. C. Anderson                                     | <i>J. Cryst. Growth</i> <b>128</b> , 672<br>(1993)       |
| Diode-Pumped, Q-Switched<br>Yb:YAG Laser  | T. Y. Fan<br>S. Klunk*<br>G. Henein*   | <i>Opt. Lett.</i> <b>18</b> , 423 (1993)                 |
| InGaAs/GaInAsP/GaInP Strained-Layer<br>Quantum Well Separate-Confinement<br>Heterostructures Grown by OMVPE                                   | S. H. Groves   | <i>J. Cryst. Growth</i> <b>124</b> , 747<br>(1992)       |

---

\*Author not at Lincoln Laboratory.

- |   |  |  |
|---|--|--|
| Degradation of Superconducting Tunnel Junction Characteristics with Increasing Barrier Transparency                                   | A. W. Kleinsasser*<br>F. M. Rammo*<br>M. Bhushan   | <i>Appl. Phys. Lett.</i> <b>62</b> , 1017 (1993)   |
| Surface-Imaged Silicon Polymers for 193-nm Excimer Laser Lithography  | R. R. Kunz<br>M. W. Horn<br>G. M. Wallraff*<br>P. A. Bianconi*<br>R. D. Miller*<br>R. B. Goodman<br>D. A. Smith*<br>J. R. Eshelman*<br>E. J. Ginsberg* | <i>Jpn. J. Appl. Phys.</i> <b>31</b> , 4327 (1992) |
| The Role of Hydrogen in Excimer-Laser-Induced Damage of Fused Silica  | D. H. Levy*<br>K. K. Gleason*<br>M. Rothschild<br>J. H. C. Sedlacek  | <i>J. Appl. Phys.</i> <b>73</b> , 2809 (1993)      |
| Optical Materials for Excimer Laser Applications  | M. Rothschild  | <i>Opt. Photon. News</i> <b>4</b> (5), 8 (1993)    |
| Excimer Laser Induced Degradation in Bulk Fused Silica  | M. Rothschild<br>J. H. C. Sedlacek   | <i>Proc. SPIE</i> <b>1935</b> , 80 (1992)          |
| Studies of Carrier Heating in InGaAs/AlGaAs Strained-Layer Quantum Well Diode Lasers Using a Multiple Wavelength Pump Probe Technique | C.-K. Sun*<br>H. K. Choi<br>C. A. Wang<br>F. G. Fujimoto*  | <i>Appl. Phys. Lett.</i> <b>62</b> , 747 (1993)    |
| InGaAs-AlGaAs Strained Quantum-Well Diode Lasers  | C. A. Wang<br>H. K. Choi<br>J. N. Walpole<br>E. S. Kintzer<br>S. R. Chinn<br>D. Z. Tsang<br>J. D. Woodhouse<br>J. P. Donnelly                          | <i>Proc. SPIE</i> <b>1788</b> , 11 (1993)          |

---

\*Author not at Lincoln Laboratory.

**Radiative Substrate Heating for High- $T_c$   
Superconducting Thin-Film Deposition:  
Film-Growth-Induced Temperature  
Variation**

A. C. Westerheim  
B. I. Choi\*  
M. I. Flik\*  
M. J. Cima\*  
R. L. Slattery  
A. C. Anderson

*J. Vac. Sci. Technol. A*  
**10, 3407 (1992)**

# ACCEPTED FOR PUBLICATION

**Calculated Room-Temperature Threshold  
Current Densities for the Visible II-VI  
ZnCdSe/ZnSe Semiconductor Quantum-  
Well Lasers**

R. L. Aggarwal  
J. J. Zayhowski  
B. Lax

*Appl. Phys. Lett.*

**Application of Radiative Renormalization  
to Strong Field Resonant Nonlinear  
Optical Interactions**

O. Blum\*  
T. K. Gustafson\*  
P. L. Kelley

*Phys. Rev. A*

**Photonic-Crystal Planar Antennas**

E. R. Brown

*ARO Res. Highlights*

**CW Operation of Monolithic Arrays of  
Surface-Emitting Folded-Cavity  
InGaAs/AlGaAs Diode Lasers**

J. P. Donnelly  
W. D. Goodhue  
C. A. Wang  
R. J. Bailey  
G. A. Lincoln  
G. D. Johnson  
L. J. Missaggia  
J. N. Walpole

*IEEE Photon. Technol. Lett.*

**Comparison of Liquid- and Vapor-Phase  
Silylation Processes for 193-nm  
Positive-Tone Lithography**

M. A. Hartney  
R. R. Kunz  
L. Eriksen  
D. C. LaTulipe\*

*Opt. Eng.*

**A Comparison of Etching Tools for  
Resist Pattern Transfer**

M. W. Horn  
M. A. Hartney  
R. R. Kunz

*Opt. Eng.*

---

\*Author not at Lincoln Laboratory.

**193-nm Resists and Lithography**

R. R. Kunz  
R. D. Allen\*  
M. A. Hartney  
M. W. Horn  
C. L. Keast  
M. Rothschild  
D. C. Shaver  
G. M. Wallraff\*

*Polym. Adv. Technol.*

**Acid-Catalyzed Single-Layer Resists for ArF Lithography**

R. R. Kunz  
R. D. Allen\*  
W. D. Hinsberg\*  
G. M. Wallraff\*

*Opt. Eng.*

**Small-Signal Admittance and Switching Measurements of the Resonant-Tunneling Diode**

J. P. Mattia  
E. R. Brown  
A. R. Calawa  
M. J. Manfra

*Appl. Phys. Lett.*

**Observation of Random-Telegraph Noise in Resonant-Tunneling Diodes**

S-H. Ng\*  
C. Surya\*  
E. R. Brown  
P. A. Maki

*Appl. Phys. Lett.*

**Laser Induced Damage in Pellicles at 193 nm**

M. Rothschild  
J. H. C. Sedlacek

*Opt. Eng.*

**Femtosecond Gain Dynamics in InGaAs/AlGaAs Strained-Layer Single-Quantum-Well Diode Lasers**

C.-K. Sun\*  
H. K. Choi  
C. A. Wang  
F. G. Fujimoto\*

*Appl. Phys. Lett.*

**PRESENTATIONS†**

**Diamond Field-Emitters for Flat-Panel Displays**

J. C. Twichell  
M. W. Geis

Program Review,  
DARPA High Definition  
Systems Information  
Exchange Conference,  
Arlington, Virginia,  
1-4 February 1993

\*Author not at Lincoln Laboratory.

†Titles of presentations are listed for information only. No copies are available for distribution.

**Diamond Review**

**M. W. Geis  
J. C. Twichell**

**Workshop on Characterizing  
Diamond Films II,  
Gaithersburg, Maryland,  
24–25 February 1993**

**Comparison of Liquid- and Vapor-Phase  
Silylation Processes for 193-nm  
Positive-Tone Lithography**

**M. A. Hartney  
R. R. Kunz  
L. M. Eriksen  
D. C. LaTulipe\***

**Experiment and Simulation of  
Sub-0.25- $\mu$ m Resist Processes  
for 193-nm Lithography**

**R. R. Kunz  
M. A. Hartney  
R. W. Otten, Jr.**

**SPIE Symposium on  
Microlithography '93,  
San Jose, California,  
28 February–5 March 1993**

**Design of Acid-Catalyzed  
Single-Layer Resists for ArF  
Lithography**

**R. R. Kunz  
G. M. Wallraff\*  
R. D. Allen\*  
W. D. Hinsberg\***

**Advanced Devices Fabricated with  
Chlorine Ion-Beam-Assisted Etching**

**W. D. Goodhue**

**Lincoln Laboratory  
Technical Seminar Series,  
University of Illinois,  
Urbana, Illinois,  
3 March 1993**

**193 Nanometer Lithography  
and Beyond**

**R. R. Kunz**

**Informal Seminar, IBM,  
San Jose, California,  
5 March 1993**

**Transition from Optical Interconnections  
to Digital Computing**

**R. C. Williamson**

**Optical Computing,  
Palm Springs, California,  
16–19 March 1993**

**Adjusting Trimethylgallium  
Injection Time to Obtain Atomic  
Layer Epitaxy of GaAs Between  
425 and 500°C**

**C. A. Wang  
D. M. Tracy**

**Sixth Biennial Workshop on  
Organometallic Vapor Phase  
Epitaxy,  
Palm Springs, California,  
21–25 March 1993**

---

**\*Author not at Lincoln Laboratory.**

Measurement of Optical Damage in  
LiNbO<sub>3</sub> Waveguide Devices

G. E. Betts  
F. J. O'Donnell  
K. G. Ray

Integrated Photonics Research,  
Palm Springs, California,  
22-24 March 1993

Plasma Oscillation Signature in the  
Quasistatic Current-Voltage  
Characteristics of Coupled Josephson  
Junctions

K. A. Delin  
A. W. Kleinsasser\*

Measurements on Superconducting  
Tunnel Junctions with High Barrier  
Transparency

A. W. Kleinsasser\*  
R. Miller\*  
K. A. Delin

Modified Two-Fluid Model for  
Superconductors: Surface Resistance

D. S. Linden\*  
T. P. Orlando\*  
W. G. Lyons

March Meeting of American  
Physical Society,  
Seattle, Washington,  
22-26 March 1993

Measured Nonlinear Surface Impedance  
and Coupled Grain Model for  
YBa<sub>2</sub>Cu<sub>3</sub>O<sub>7-x</sub> Thin Films

P. P. Nguyen\*  
D. E. Oates  
G. Dresselhaus

Application of Frequency-Domain  
Analysis to RHEED Oscillation Data:  
Time Dependence of AlGaAs Growth  
Rates

G. W. Turner  
S. J. Eglash

Lincoln Laboratory  
Technical Seminar Series,  
University of Virginia,  
Charlottesville, Virginia,  
26 March 1993

Diamond Review

M. W. Geis  
J. C. Twichell

Seminar, Johns Hopkins  
University,  
Laurel, Maryland,  
26 March 1993

MIT Lincoln Laboratory Source  
Development

T. Y. Fan

Electro-Optic Countermeasures  
Colloquium VIII,  
Edinburgh, Scotland,  
29 March-2 April 1993

InGaAs-GaAs Strained-Layer  
Materials for Optoelectronic Devices

C. A. Wang

Optics and Quantum Electronics  
Seminar Series,  
Cambridge, Massachusetts,  
7 April 1993

---

\*Author not at Lincoln Laboratory.



**Pattern Transfer of Surfaced-Imaged  
Resists Using a Helicon Etch  
Reactor**

**M. W. Horn  
M. A. Hartney  
R. R. Kunz  
B. M. Chapman\*  
C. F. A. VanOs\*  
I. DeLaRosa\*  
D. R. Pirkle\***

**Seminar, SPIE Photolithography  
User Group and  
American Vacuum  
Society Plasma Etch  
User Group,  
Palo Alto, California,  
8 April 1993**

**GaSb-Based Diode Lasers for 2-  
to 5- $\mu$ m Emission**

**D. L. Spears**

**Lincoln Laboratory  
Technical Seminar Series,  
University of Connecticut,  
Storrs, Connecticut,  
9 April 1993**

**Coherent Microwave Generation  
with an LTG-GaAs Photomixer**

**E. R. Brown  
K. A. McIntosh  
F. W. Smith  
K. B. Nichols  
M. J. Manfra  
C. L. Dennis**

**Low-Frequency and Phase Noise  
in MESFETs with and without LTG-  
GaAs Passivation Layers**

**Y. Lin\*  
A. D. van Rheenen\*  
C. L. Chen  
F. W. Smith**

**1993 Spring Materials Research  
Society Meeting,  
San Francisco, California,  
12-16 April 1993**

**YBa<sub>2</sub>Cu<sub>3</sub>O<sub>7-x</sub> Thin Films with Large  
Power Handling Capability**

**D. E. Oates  
A. C. Anderson  
A. C. Westerheim  
P. P. Nguyen**

**Mid-Infrared Diode Lasers**

**D. L. Spears**

**Sixth Annual Diode Laser  
Technology Program,  
Kirtland Air Force Base,  
Albuquerque, New Mexico,  
20-22 April 1993**

---

**\*Author not at Lincoln Laboratory.**

**Optical Interconnections for Digital  
Systems**

**D. Z. Tsang**

**Lincoln Laboratory  
Technical Seminar Series,  
University of Arizona,  
Tucson, Arizona,  
26 April 1993**

**Multiple-Quantum-Well Optoelectronic  
Devices**

**B. F. Aull**

**Lincoln Laboratory  
Technical Seminar Series,  
Harvard University,  
Cambridge, Massachusetts,  
27 April 1993**

## ORGANIZATION

### SOLID STATE DIVISION

A. L. McWhorter, *Head*  
I. Melngailis, *Associate Head*  
E. Stern, *Associate Head*  
D. C. Shaver, *Assistant Head*  
J. F. Goodwin, *Assistant*  
  
D. J. Ehrlich, *Senior Staff*  
N. L. DeMeo, Jr., *Associate Staff*  
J. W. Caunt, *Assistant Staff*  
K. J. Challberg, *Administrative Staff*

### SUBMICROMETER TECHNOLOGY

M. Rothschild, *Leader*  
T. M. Lyszczarz, *Assistant Leader*

Astolfi, D. K.	Hartney, M. A.
Craig, D. M.	Horn, M. W.
Dennis, C. L.	Keast, C. L.
DiNatale, W. F.	Kunz, R. R.
Doran, S. P.	Maki, P. A.
Efremow, N. N., Jr.	Melngailis, J.†
Forte, A. R.	Sedlacek, J. H. C.
Geis, M. W.	Twichell, J. C.
Goodman, R. B.	Uttaro, R. S.

### QUANTUM ELECTRONICS

A. Sanchez-Rubio, *Leader*  
T. Y. Fan, *Assistant Leader*

Aggarwal, R. L.	Hsu, L.*
Cook, C. C.	Jeys, T. H.
Daneu, V.	Kelley, P. L.‡
DeFeo, W. E.	Le, H. Q.
DiCecca, S.	Nabors, C. D.
Dill, C. D., III	Ochoa, J. R.
Hancock, R. C.	Zayhowski, J. J.
Hotaling, T. C.	

### ELECTRONIC MATERIALS

B-Y. Tsauro, *Leader*  
D. L. Spears, *Assistant Leader*

Anderson, C. H., Jr.	Krohn, L., Jr.
Button, M. J.	Marino, S. A.
Chen, C. K.	Mastromattei, E. L.
Choi, H. K.	McGilvary, W. L.
Connors, M. K.	Nitishin, P. M.
Fahey, R. E.	Pantano, J. V.
Finn, M. C.	Reinold, J. H., Jr.
Harman, T. C.	Turner, G. W.
Iseler, G. W.	Wang, C. A.

### HIGH SPEED ELECTRONICS

R. A. Murphy, *Leader*  
M. A. Hollis, *Assistant Leader*

Bozler, C. O.	Manfra, M. J.
Brown, E. R.	Mathews, R. H.
Chen, C. L.	Mattia, J. P.*
Clifton, B. J.‡	McIntosh, K. A.
Crenshaw, D. L.*	Nichols, K. B.
Goodhue, W. D.	Parker, C. D.
Harris, C. T.	Rabe, S.
Lincoln, G. A., Jr.	Rathman, D. D.
Mahoney, L. J.	Smith, F. W., III

\* Research Assistant

† Part Time

‡ Leave of Absence

## ELECTROOPTICAL DEVICES

R. C. Williamson, *Leader*  
L. M. Johnson, *Assistant Leader*

Aull, B. F.  
Bailey, R. J.  
Betts, G. E.  
Donnelly, J. P.  
Golubovic, B.\*  
Groves, S. H.  
Hovey, D. L.  
Liau, Z. L.  
Lind, T. A.  
Missaggia, L. J.

Mull, D. E.  
O'Donnell, F. J.  
Palmacci, S. T.  
Palmateer, S. C.  
Reeder, R. E.  
Roussell, H. V.  
Tsang, D. Z.  
Walpole, J. N.  
Woodhouse, J. D.

## ANALOG DEVICE TECHNOLOGY

R. W. Ralston, *Leader*  
T. C. L. G. Sollner, *Assistant Leader*  
A. C. Anderson, *Senior Staff*  
A. M. Chiang, *Senior Staff*

Abusch, D. M.\*  
Arsenault, D. R.  
Boisvert, R. R.  
Brogan, W. T.  
Curd, D. R.\*  
Delin, K. A.  
Denneno, J. M.  
Fitch, G. L.  
Goldinger, J. E.\*  
Green, J. B.†  
Holtham, J. H.

LaFranchise, J. R.  
Linden, D. S.\*  
Lyons, W. G.  
Macedo, E. M., Jr.  
Mankiewich, P. M.  
Oates, D. E.  
Sage, J. P.  
Seaver, M. M.  
Slattery, R. L.  
Tam, K.\*  
Whitley, D. B.

## MICROELECTRONICS

E. D. Savoye, *Leader*  
B. B. Kosicki, *Assistant Leader*  
B. E. Burke, *Senior Staff*

Clark, H. R., Jr.  
Daniels, P. J.  
Doherty, C. L., Jr.  
Dolat, V. S.  
Donahue, T. C.

Felton, B. J.  
Gregory, J. A.  
Johnson, K. F.  
Loomis, A. H.  
McGonagle, W. H.

Mountain, R. W.  
Percival, K. A.  
Pichler, H. H.  
Reich, R. K.  
Young, D. J.

---

\* Research Assistant  
† Leave of Absence

# 1. ELECTROOPTICAL DEVICES

## 1.1 MONOLITHIC OPTOELECTRONIC TRANSISTOR

A new optoelectronic switching and logic device, the monolithic optoelectronic transistor (MOET), has been demonstrated. It uses multiple-quantum-well (MQW) p-i-n diodes as both photodetectors for optical input and reflection modulators for optical output. High modulator contrast is achieved by using an asymmetric Fabry-Perot cavity structure [1]. The switching action is obtained with a double-barrier resonant-tunneling diode (RTD).

The circuit of the simplest version of the MOET is shown in Figure 1-1(a). The RTD, which is connected in series with the input detector, has a region of negative differential resistance in its current-voltage (I-V) characteristic, as shown in Figure 1-1(b). When the detector photocurrent exceeds the peak current of the RTD, the RTD operating voltage abruptly increases, turning on a field-effect transistor (FET) and causing a much larger voltage increase across the modulator. This amplification is illustrated in Figure 1-1(c). The wavelength at which the modulator is illuminated is somewhat longer than that of the MQW exciton absorption peak, so the quantum-confined Stark effect [2] causes it to switch from a high- to a low-reflectivity state. When the detector photocurrent subsequently decreases to below the valley current of the RTD, the RTD switches back to low voltage, turning off the FET and switching the modulator back to a high-reflectivity state. The optical transfer characteristic is inverting and has some hysteresis determined by the peak-to-valley current ratio of the RTD. Figure 1-1(d) shows the expected optical transfer characteristic. Because of the saturation of the electronic circuit, the MOET has saturated "on" and "off" output intensity levels. It is possible to design the circuit elements so that the modulator can be illuminated at much greater power levels than the detector, giving the MOET large-signal optical gain.

The circuit shown in Figure 1-1(a) was fabricated monolithically on a <100> semi-insulating GaAs substrate by gas-source molecular beam epitaxy, resulting in a structure whose cross section is illustrated in Figure 1-2. The epitaxial layers include, in order of growth, a dielectric mirror (the bottom reflector of the Fabry-Perot cavity), an n-i-p structure with an MQW in the "i" region (for the detector and modulator), an undoped GaAs buffer layer (to reduce leakage current and backgating effects in the FET), an n-type GaAs layer (the FET channel), the RTD structure, and finally, a contact layer of  $n^+$ -type GaAs. The FET channel is 3  $\mu\text{m}$  long and 100  $\mu\text{m}$  wide. The detector and modulator areas are each  $150 \times 150 \mu\text{m}$ .

The optical transfer characteristic of the MOET was measured by illuminating the detector and the modulator with AlGaAs laser diodes. Figure 1-3 shows two transfer characteristics generated using different bias voltages on the RTD cathode. For sufficiently low absolute values of the RTD bias, turn-on and turn-off of the FET occur in the positive resistance region of the RTD I-V curve at currents below the valley current. For sufficiently high absolute values, they occur in the positive resistance region at currents above the peak current, as seen in Figure 1-3(a). In both cases there is a region of finite slope in the optical transfer characteristic and no hysteresis. The quasi-sigmoidal transfer characteristic of Figure 1-3(a) demonstrates the potential of the MOET for optoelectronically implemented neural networks.

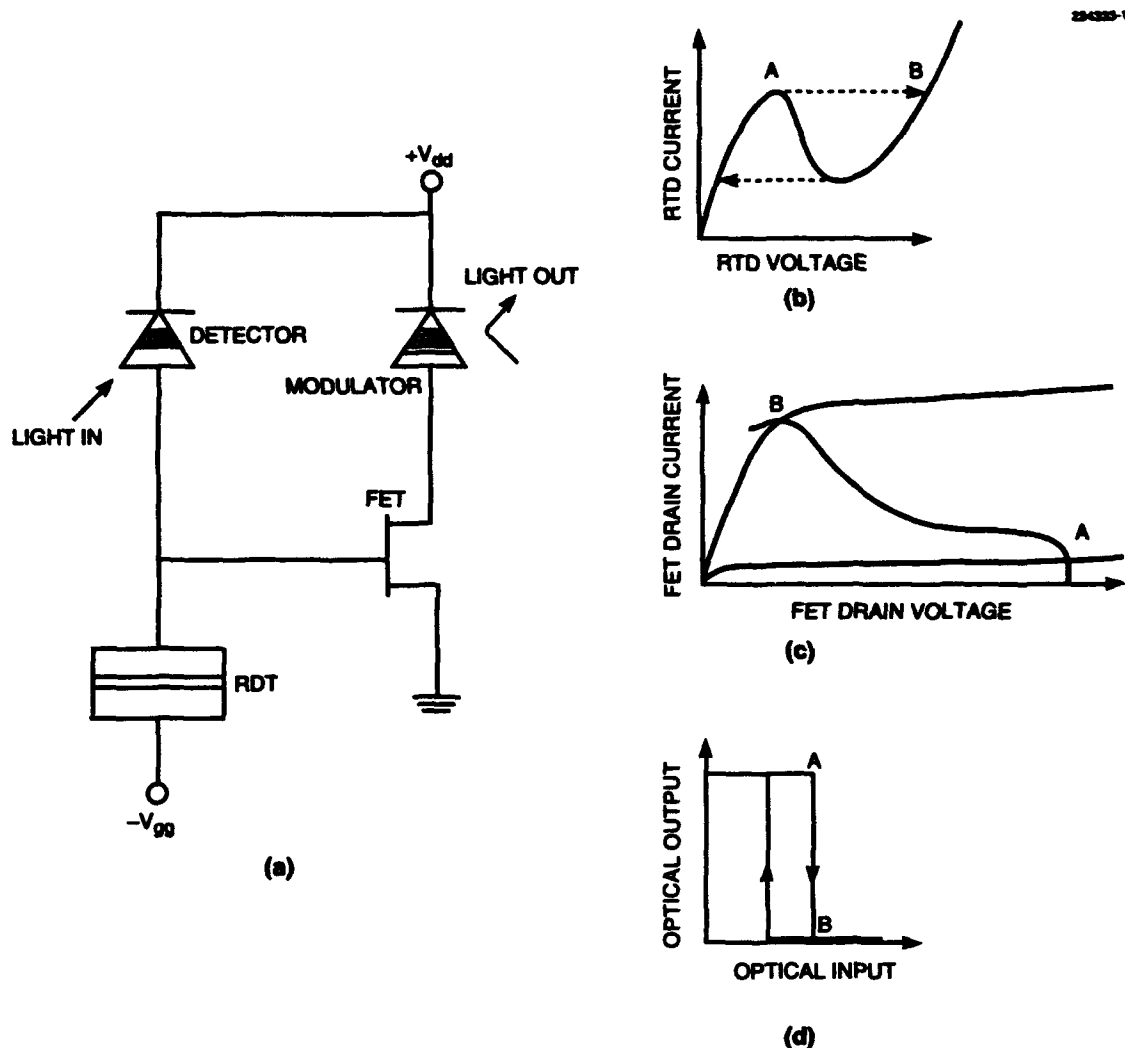


Figure 1-1. (a) Circuit of simplest version of monolithic optoelectronic transistor (MOET). (b) Current-voltage (I-V) characteristic of resonant-tunneling diode (RTD). The operating points just before and just after the field-effect transistor (FET) turns on are indicated by points A and B, respectively. The dashed arrows show the abrupt changes in operating point that occur at the switching points of the MOET device. (c) Drain-source I-V characteristics of the FET just before and just after it turns on. The I-V characteristic of the illuminated modulator is included as a nonlinear load line. In its low-reflectivity state, the modulator is highly absorbing and produces much more photocurrent than in the high-reflectivity state. (d) Expected optical transfer characteristic of the MOET.

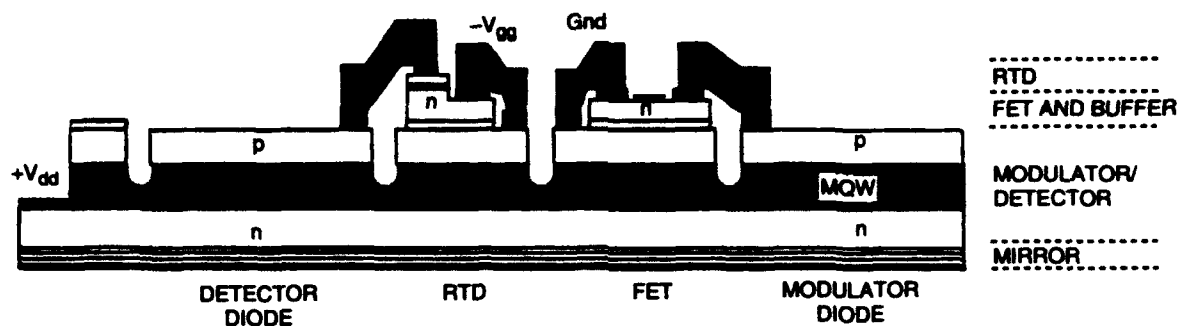


Figure 1-2. Cross section showing structure of MOET after circuit fabrication is complete. The only metallization connection not shown is from the p side of the detector to the gate of the FET. Also not shown is the silicon nitride layer.

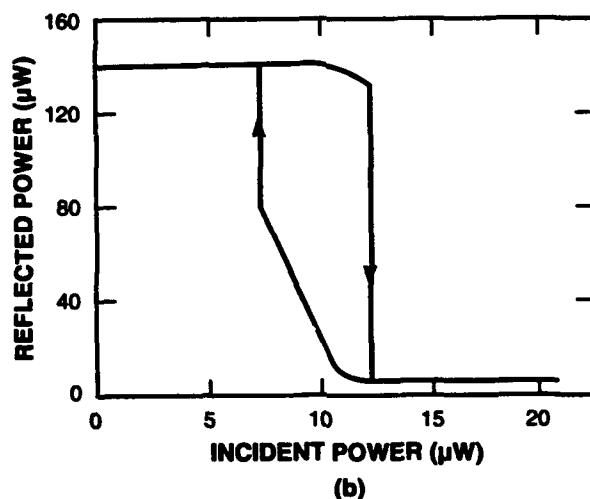
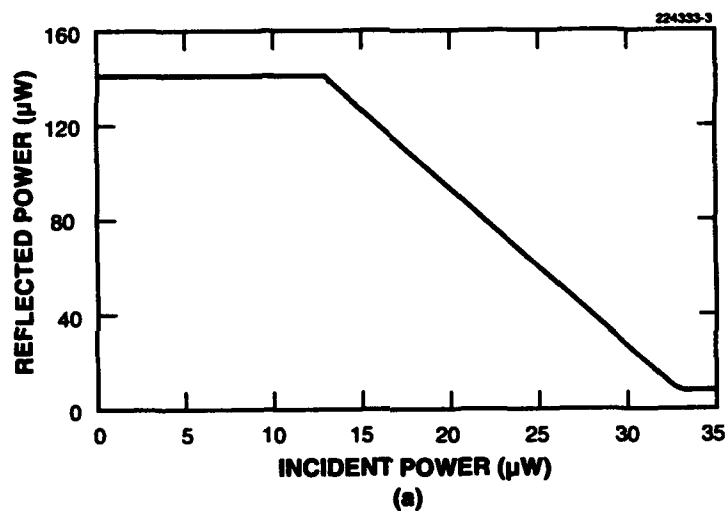


Figure 1-3. Measured optical transfer characteristic of MOET at modulator illumination levels giving on-state output power of 140  $\mu\text{W}$  for (a)  $V_{gg} = 5.8 \text{ V}$  and (b)  $V_{gg} = 5.4 \text{ V}$ .

For intermediate values of RTD bias, FET switching occurs at RTD voltages in the valley of the RTD I-V curve. Abrupt switching transitions and hysteresis appear, as seen in Figure 1-3(b). The output turn-off and turn-on occur at input powers of 12.5 and 7.5  $\mu\text{W}$ , respectively. The output contrast ratio in this measurement is roughly 24:1. The modulator on the same device has a peak contrast ratio of over 55:1 when its reflectivity is measured with a monochromator. By defining optical gain as the change in output power divided by the input power required to produce that change, the maximum gain obtained is 10.7 and occurs at modulator illumination levels giving an on-state output power of  $\sim 140 \mu\text{W}$ . The voltage change provided by the RTD and the transconductance of the FET limit the optical gain.

B. F. Aull	K. B. Nichols
P. A. Maki	S. C. Palmateer
E. R. Brown	T. A. Lind

## REFERENCES

1. M. Whitehead, A. Rivers, G. Parry, J. S. Roberts, and C. Button, *Electron. Lett.* **25**, 984 (1989).
2. D. A. B. Miller, D. S. Chemla, T. C. Damen, A. C. Gossard, W. Wiegmann, T. H. Wood, and C. A. Burrus, *Phys. Rev. B* **32**, 1043 (1985).



## 2. QUANTUM ELECTRONICS

### 2.1 HOLMIUM LASER PUMPED BY 1.9- $\mu\text{m}$ DIODE LASER

A widespread trend is evident toward using solid state lasers in the eyesafe band ( $> 1.4 \mu\text{m}$ ) for a variety of military applications, including rangefinders, target designators, and battlefield simulators. Civil applications of eyesafe lasers include laser surgery and laser radar for wind and turbulence sensing. Many of these applications require short ( $< 10 \text{ ns}$ ) pulse operation. Direct pumping at  $1.91 \mu\text{m}$  of the  $\text{Ho } ^5I_7-^5I_8$  transition (emitting at  $2.1 \mu\text{m}$ ) [1] is an attractive alternative to the currently employed Tm [2] and co-doped Tm, Ho [3] lasers, as it potentially avoids the problems with upconversion, low effective storage time, multipulsing, and optical damage observed in these systems. This scheme also has the advantage of relatively low thermal loading of the gain medium, which results in low thermo-optic distortion, and thus has the potential for scaling to high powers. Based on the quantum defect alone, the thermal load is only 9% of the absorbed pump power for Ho:YAG, a factor of 3 lower than the value of 25% for a co-doped Tm, Ho laser pumped at 785 nm.

We have recently demonstrated diode lasers emitting at  $1.9 \mu\text{m}$ , the wavelength required for pumping  $\text{Ho}^{3+}$  in YAG and YLF hosts [4]. Single-ended output power up to 1.3 W CW has been obtained for room-temperature operation of a  $300\text{-}\mu\text{m}$ -wide device. These new lasers, which have a multiple-quantum-well structure with GaInAsSb wells and AlGaAsSb barriers, are grown by molecular beam epitaxy on GaSb substrates. The bandwidth of the emission is  $\sim 7 \text{ nm}$  at high power levels.

This diode laser was used to directly diode pump and achieve lasing on the  $^5I_7-^5I_8$  transition of Ho:YAG for the first time. A pump beam from a GaInAsSb diode laser was focused to a  $135 \times 276\text{-}\mu\text{m}$  spot (equivalent Gaussian radius with 10–90% transmitted-power clip levels) with vertical and horizontal beam-quality parameters ( $M^2$ ) of 75 and 332 times diffraction limited, respectively, and a residual astigmatism of  $330 \mu\text{m}$  or less. The low beam quality is largely due to the use of two cylindrical singlet lenses in the pump optical system. The result is poor mode overlap with the Ho laser, which limits efficiency.

The Ho laser consisted of a 1.02-mm-thick 4% Ho:YAG crystal mounted on a thermoelectrically cooled stage in a near-hemispherical cavity. The crystal had a multilayer dichroic coating on one side (98% transmission at  $1.91 \mu\text{m}$ , highly reflecting at  $2.1 \mu\text{m}$ ) and was antireflection coated on the other. The 5-cm radius of curvature output coupler had 1% transmission at  $2.1 \mu\text{m}$ . The cavity mode spot size in the crystal was measured to be  $60 \mu\text{m}$ .

Diode pump power incident on the crystal was limited to a maximum of 485 mW because of losses from uncoated lenses in the pump beam-shaping system. The ratio of absorbed pump power to incident pump power ranged from 22% at high diode powers ( $\sim 1 \text{ W}$ ) to 33% at lower powers, since broadening of the pump's emission spectrum occurs with increasing drive current and optical power, which reduces the effective absorbance of the crystal. Figure 2-1 shows the laser output power as a function of absorbed pump power. The slope efficiency well above threshold is 47%, demonstrating that reasonable extraction efficiency can be had despite the difference of pump and cavity mode spot sizes. The crystal temperature was held at  $-51^\circ\text{C}$  for these measurements.

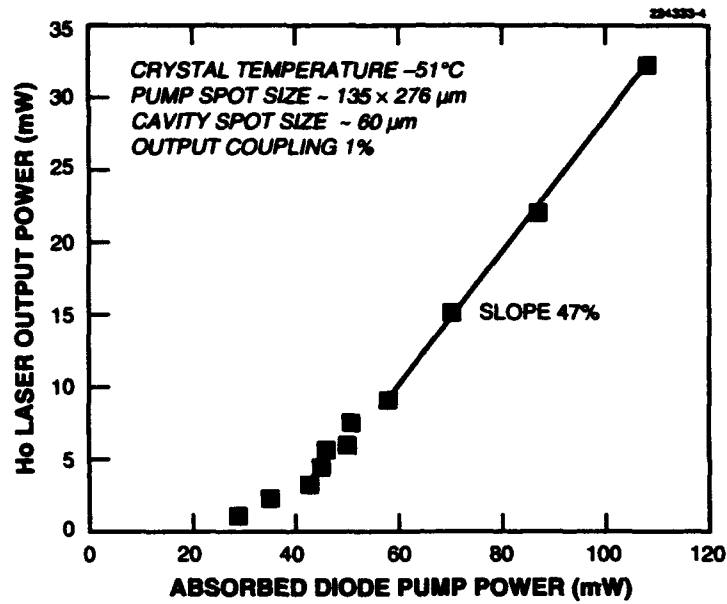


Figure 2-1. Ho laser output vs absorbed pump power. The line fit is to the last four points only.

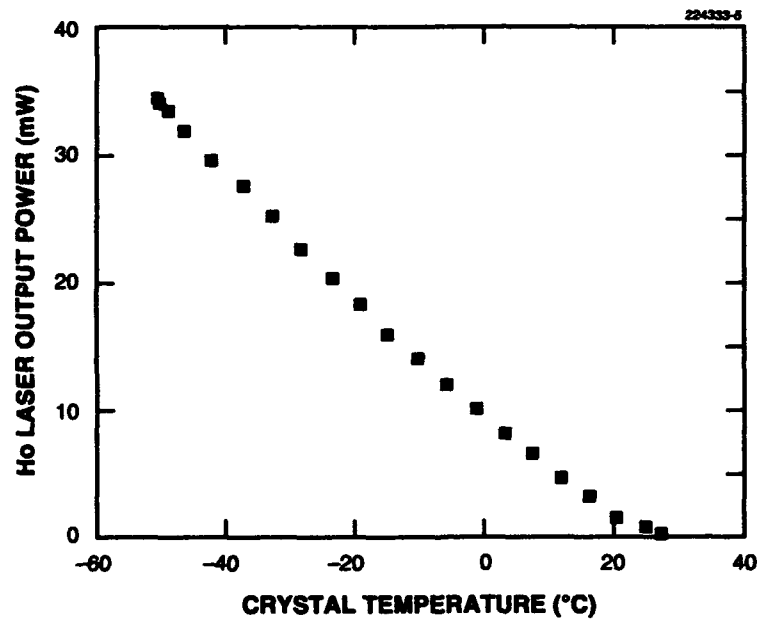


Figure 2-2. Ho laser output vs crystal temperature.

Figure 2-2 shows the effect of changes in crystal temperature on the Ho laser output power, with the incident pump power held at its maximum value of 485 mW. The measured temperature is that of the crystal mount, and the true temperature in the laser mode volume is somewhat higher. Laser reabsorption loss increases with temperature owing to the quasi-three-level nature of the transition, and this causes the laser to go below threshold for temperatures greater than 27°C. We expect to achieve efficient room-temperature operation with reduced pump spot size and increased pump power.

C. D. Nabors

H. K. Choi

J. R. Ochoa

G. W. Turner

T. Y. Fan

## REFERENCES

1. R. C. Stoneman and L. Esterowitz, *Opt. Lett.* **17**, 736 (1992).
2. T. S. Kubo and T. J. Kane, *IEEE J. Quantum Electron.* **28**, 1033 (1992).
3. B. T. McGuckin, R. T. Menzies, and H. Hemmati, *Appl. Phys. Lett.* **59**, 2926 (1991).
4. H. K. Choi and S. J. Eglash, *Appl. Phys. Lett.* **61**, 1154 (1992).

### 3. MATERIALS RESEARCH

#### 3.1 MBE GROWTH AND CHARACTERIZATION OF $\text{PbTe}_{0.8}\text{Se}_{0.2}$ FILMS

Films of  $\text{PbTe}_{0.8}\text{Se}_{0.2}$  have been grown by molecular beam epitaxy (MBE) on  $18 \times 18 \times 1$ -mm, [111]-oriented, cleaved, single-crystal  $\text{BaF}_2$  substrates for evaluation as one of the components in a thermoelectric superlattice. Record high Seebeck coefficients or thermopowers of  $390 \mu\text{V/K}$  at 300 K and record low electron carrier concentrations of  $1.1 \times 10^{16} \text{ cm}^{-3}$  at 77 K were obtained. Over the past four decades the Pb chalcogenides have been examined for thermoelectric energy conversion applications. Pb-salt alloy films have also been investigated over the past three decades for use in infrared detectors and diode lasers [1]. Some of the physical properties for the present undoped films are better than the previously reported values for undoped epitaxial  $\text{PbTeSe}$  with alloy compositions significantly different from the binary components [2]. Furthermore, the carrier type and concentration vary with the Te beam-equivalent pressure (BEP) in a smooth and understandable manner.

The  $\text{PbTe}_{0.8}\text{Se}_{0.2}$  films were grown using a modified Varian 360 MBE system (equipped with a  $\text{PbTe}_{0.8}\text{Se}_{0.2}$  effusion cell and a Te effusion cell) which has ion-pumped load-lock and growth chambers. The base pressure in the growth chamber during growth was maintained in the range  $3\text{--}5 \times 10^{-10}$  Torr. The growth chamber is equipped with a quadrupole mass analyzer, ion gauges for monitoring beam flux and base pressure, and a reflection high-energy electron diffraction (RHEED) system.

This material was prepared as follows. Initially, a 300-g charge containing as-received semiconductor-grade Pb, Te, and Se in chunk form was placed in a carbonized fused-silica ampoule in  $\text{Pb}_{0.5}(\text{Te}_{0.8}\text{Se}_{0.2})_{0.5}$  proportions. After the ampoule was loaded, it was evacuated with a diffusion or turbomolecular pump and sealed. The ampoule was then placed inside a fused-silica protection tube, and the tube was in turn evacuated, back filled with argon to a pressure of 0.25 atm, and sealed. Next, the sealed protection tube was placed in a resistance furnace with the ampoule at the center of the furnace, and the region containing the ampoule was heated to about  $950^\circ\text{C}$ , which is about  $50^\circ\text{C}$  above the liquidus temperature. After heating, the ampoule was slowly lowered out of the Bridgman furnace. The reacted and homogenized  $\text{PbTe}_{0.8}\text{Se}_{0.2}$  was then cooled to room temperature and placed in the MBE effusion cell crucible in chunk form for growth. A second effusion cell was loaded with semiconductor-grade Te.

Following the growth of a nucleation layer at  $\sim 350^\circ\text{C}$  for 75 s, the substrate temperature was lowered to a value in the range  $250\text{--}350^\circ\text{C}$  during the rest of the growth. Growth rates were typically  $1 \mu\text{m/h}$ . The  $\text{PbTe}_{0.8}\text{Se}_{0.2}$  effusion cell temperature was held constant at  $530^\circ\text{C}$ , whereas four values of the Te effusion cell temperature were used: 250, 280, 290, and  $320^\circ\text{C}$ .

The lattice constant of the cubic  $\text{BaF}_2$  substrate is 0.6201 nm as calculated from the data shown in Figure 3-9(a) of Ref. [3], which is in good agreement with the literature value of 0.6200 nm. From x-ray diffraction (XRD) results along the [444] crystallographic direction, shown in Figure 3-1 of the present report, the lattice constant of a typical MBE-grown  $\text{PbTe}_{0.8}\text{Se}_{0.2}$  epilayer is calculated to be 0.6386 nm, which is only 3.0% larger than the lattice constant of  $\text{BaF}_2$ . The clear resolution of the two  $K_\alpha$  lines in Figure 3-1 indicates that good-quality epilayer growth and good alloy homogeneity have been achieved.

Figure 3-2(a) shows an optical photomicrograph of a typical (111) cleaved cross section of a 7- $\mu\text{m}$ -thick  $\text{PbTe}_{0.8}\text{Se}_{0.2}$  layer, and Figure 3-2(b) is a photomicrograph of the (111) as-grown surface of a sample for which the Te effusion cell temperature was 280°C. The surface morphology is smooth, except for small cleavage steps in the  $\text{BaF}_2$  substrate, and thermal dislocation etch pits are observed over the entire surface. The RHEED observations along with the XRD and surface morphology results indicate that high-quality epilayers are being grown.

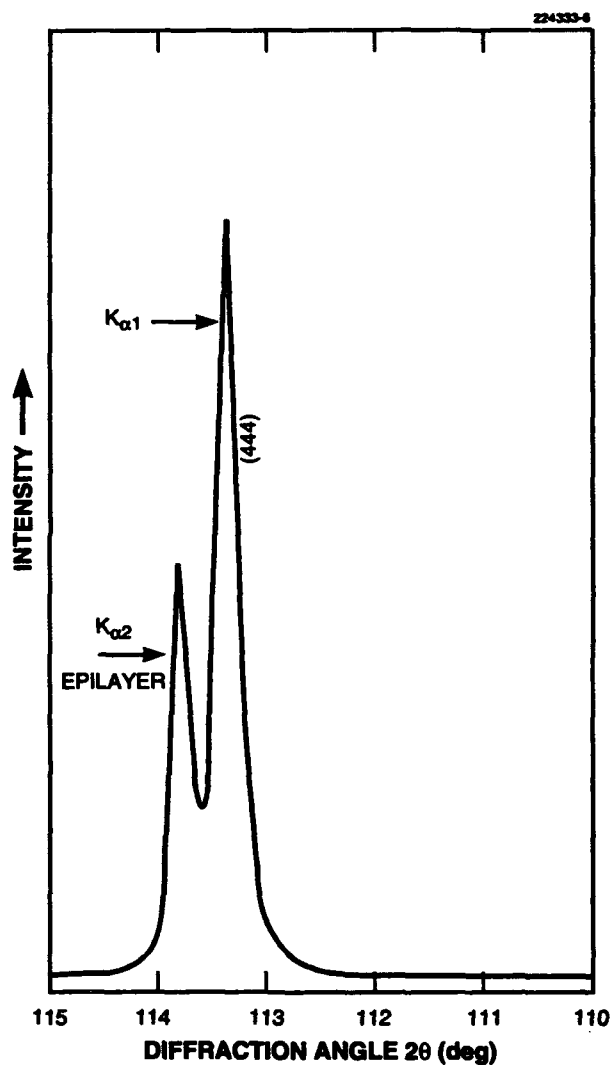
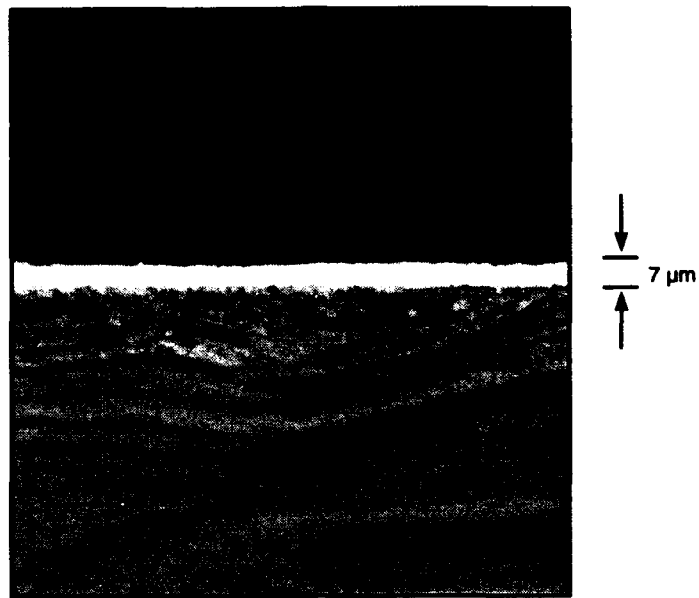


Figure 3-1. [444] x-ray diffraction lines for  $\text{PbTe}_{0.8}\text{Se}_{0.2}$  film grown by molecular beam epitaxy (MBE).



(a)



(b)

Figure 3-2. Optical micrographs of (a) cleaved cross section of  $\text{PbTe}_{0.8}\text{Se}_{0.2}$  MBE-grown film on  $(111) \text{Ba}_2\text{F}$  substrate and (b) as-grown surface of  $\text{PbTe}_{0.8}\text{Se}_{0.2}$  film.

Hall coefficient and electrical resistivity measurements of the MBE-grown films were measured at 300 and 77 K. Also, the Seebeck coefficient was measured at room temperature. A magnetic field of 5 kG oriented perpendicular to the film plane was used for the van der Pauw Hall measurements. The Hall coefficient and the resistivity of the Pb salts, in contrast to  $\text{Bi}_{0.9}\text{Sb}_{0.1}$  [3], are isotropic. Results for 9-mm-square samples are displayed in Table 3-1. Here, the electron and hole mobility values are for the carriers along the four L-conduction and L-valence band ellipsoids, respectively. The change in carrier type as the beam flux ratio (the ratio of the  $\text{PbTe}_{0.8}\text{Se}_{0.2}$  BEP to the Te BEP) decreases is believed to occur because of a change from a predominance of excess metal defects for  $n$ -type to a predominance of excess chalcogenide defects for  $p$ -type. The results in Table 3-1 show that as the Te effusion cell temperature increases the carrier type changes from  $n$ - to  $p$ -type in a smooth manner. It is also seen in Table 3-1 that as the beam flux ratio decreases the carrier concentration of the layers decreases on the  $n$ -type side of stoichiometry and then increases on the  $p$ -type side. These results indicate that the carrier type and concentration can be controlled by varying the flux ratio.

T. C. Harman

**TABLE 3-1**  
**Physical Properties of MBE-Grown  $\text{PbTe}_{0.8}\text{Se}_{0.2}$  Films**

Sample	Te Cell Temp. (°C)	Beam Flux Ratio	300-K Mobility ( $\text{cm}^2 \text{V}^{-1} \text{s}^{-1}$ )	300-K Carrier Concentration and Type ( $\text{cm}^{-3}$ )	77-K Mobility ( $\text{cm}^2 \text{V}^{-1} \text{s}^{-1}$ )	77-K Carrier Concentration and Type ( $\text{cm}^{-3}$ )	300-K Seebeck Coefficient ( $\mu\text{V/K}$ )
T-50	250	71	110	$7 \times 10^{17}$ , $n$	—	$1.1 \times 10^{16}$ , $n$	-223
T-52	280	13	500	$2 \times 10^{17}$ , $n$	6300	$9.6 \times 10^{16}$ , $n$	-313
T-53	290	7.2	260	$6 \times 10^{16}$ , $p$	—	$5.3 \times 10^{16}$ , $p$	390
T-55	320	1.6	325	$1.4 \times 10^{17}$ , $p$	1500	$8 \times 10^{16}$ , $p$	371

## REFERENCES

1. D. L. Partin, in *Semiconductors and Semimetals*, R. K. Willardson and A. C. Beer, eds. (Academic, New York, 1991), p. 311 and references therein.
2. D. K. Hohnke and M. D. Hurley, *J. Appl. Phys.* **47**, 4975 (1976); B. A. Efimova, T. S. Stavkitskaya, L. S. Stilbans, and L. M. Sysoeva, *Sov. Phys. Solid State* **1**, 1217 (1960).
3. *Solid State Research Report*, Lincoln Laboratory, MIT, 1993:1, p. 17.

## 4. SUBMICROMETER TECHNOLOGY

### 4.1 ACID-CATALYZED SINGLE-LAYER RESIST FOR 193-nm LITHOGRAPHY

Photolithography at 193 nm using an ArF excimer laser is one of the main candidate technologies for printing devices with 0.25- $\mu\text{m}$  dimensions and below. One factor limiting the acceptance of 193-nm lithography has been the lack of suitable single-layer resists. Because of the high absorbance of phenolic resins, resists developed for deep ultraviolet (DUV) applications (248 nm) are not usable at shorter wavelengths. Therefore, resist development at 193 nm has focused primarily on surface-imaged and bilayer approaches. Until recently, the only single-layer resist that had been demonstrated to work at 193 nm was poly(methyl methacrylate) (PMMA), but its sensitivity is very low, with doses  $> 1 \text{ J/cm}^2$  required. More advanced acrylate-based systems that operate via acid-catalyzed conversion of *t*-butyl methacrylate (tBMA) into methacrylic acid (MAA) have been developed for laser direct-write applications [1],[2] at visible-laser wavelengths. These resists are easily adapted for use at 193 nm, since acrylates are semitransparent at this wavelength. Here, we describe progress toward developing such high-sensitivity, high-resolution resists. In particular, we have demonstrated that 0.1- $\mu\text{m}$  resolution is achievable with single-layer resists at 193 nm.

Our new resist contains resins synthesized by free-radical terpolymerization of tBMA, MMA, and MAA, and it meets the transparency and thermal stability requirements for single-layer resist applications. The solubility of these terpolymers can be controlled by variations in MAA content. For example, when the MAA concentration is  $\sim 20 \text{ mol}\%$  the exposed films are aqueous-base soluble only after exposure, whereas at MAA fractions approaching 30 mol% the unexposed resin itself becomes aqueous-base soluble.

Recent studies have also indicated that acrylates, as a class of resins, are less prone to airborne base contamination than are phenolic resins used for longer-wavelength resists [3]. Airborne contamination is thought to be a leading cause of the environmental instability reported for DUV resists. If these studies are further substantiated, 193-nm resists may have a clear advantage over the current generation of acid-catalyzed DUV systems.

Since the lithographic process requires acid-catalyzed chemical amplification to increase the sensitivity of the resist, the resist formulation must contain a photoacid generator (PAG) in addition to the base resin. Depending on the type used, the amount that can be added to the resist may be limited by its absorbance at 193 nm. Figure 4-1 shows the absorption coefficient measured at 194 nm as a function of acid generator loading for a poly(MMA-co-tBMA-co-MAA) terpolymer with bis(*t*-butylphenyl) iodonium triflate PAG. Also shown in the figure is the sensitivity of the resist and its dependence on loading. Figure 4-2 shows a contrast curve for a formulation containing 1 wt% of the same PAG. The contrast  $\gamma$  as determined from Figure 4-2 is 3.5. It is clear that a large window in formulation exists that will allow optimal photospeed, good contrast, and high transparency.

An optimized resist formulation was exposed using a 193-nm prototype optical stepper with 0.5 numerical aperture (NA). Figure 4-3 shows resulting features 0.3–0.5  $\mu\text{m}$  in size that were patterned with a conventional chrome-on-quartz photomask, and the results using a chromeless phase-shifting mask are illustrated in Figure 4-4 [4]. The resolution limit using a shifter-only mask is equal to  $\lambda/(4 \text{ NA})$ , which



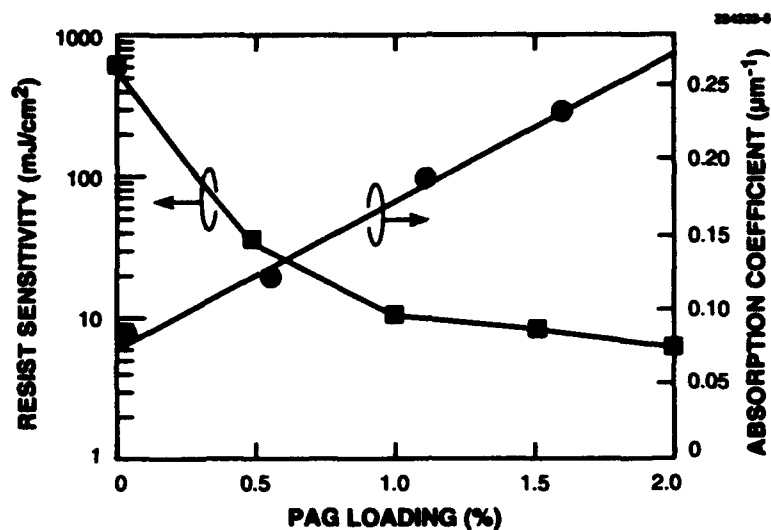


Figure 4-1. Absorption coefficient at 194 nm of poly(MMA-co-tBMA-co-MAA) terpolymer as function of photoacid generator (PAG) loading. The PAG was bis(*t*-butylphenyl) iodonium triflate. Also shown is the sensitivity of the resist vs PAG loading, after a 130°C, 1-min post-exposure bake.

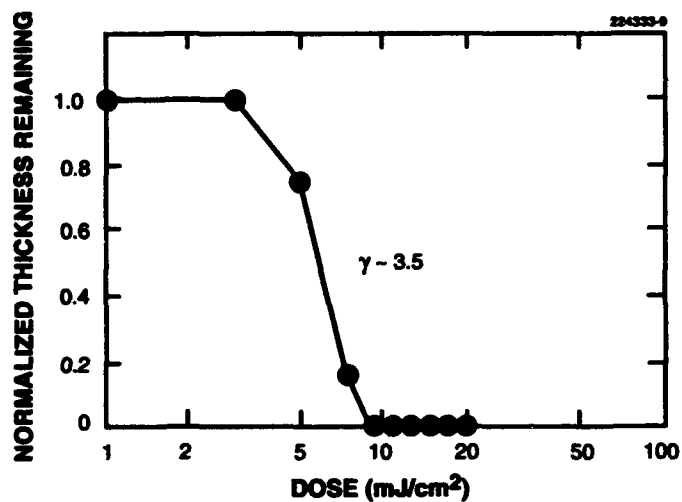
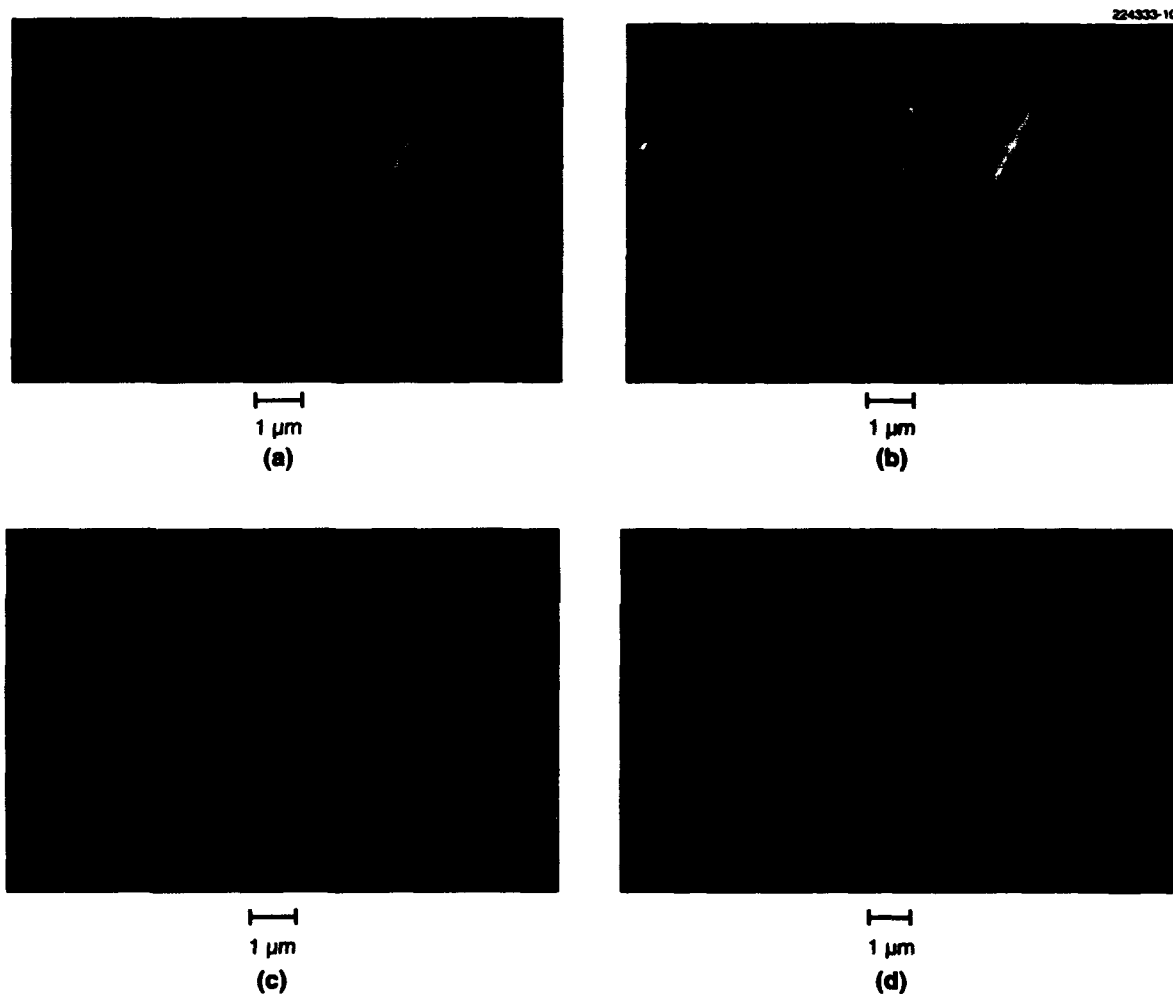
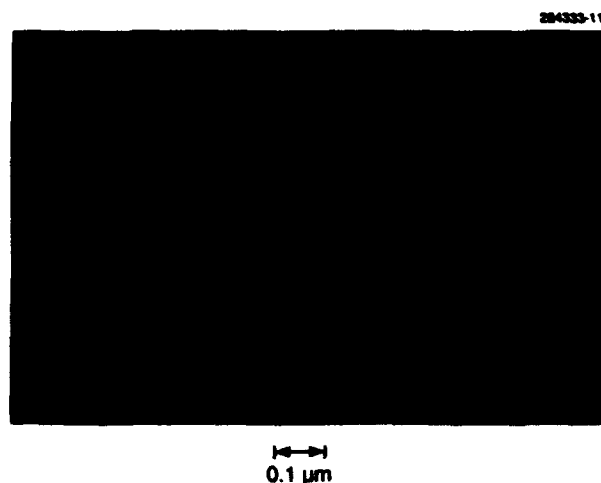


Figure 4-2. Contrast curve for poly(MMA-co-tBMA-co-MAA) with 1% bis(*t*-butylphenyl) iodonium triflate PAG, developed in 0.01-N TMAH after a 130°C, 1-min post-exposure bake.

is  $0.097\ \mu\text{m}$  for this exposure system. Figure 4-4 shows a  $0.1\text{-}\mu\text{m}$ -wide isolated line in a  $0.5\text{-}\mu\text{m}$  resist. This resolution is, we believe, the smallest ever printed in projection with optical techniques. It clearly shows that the intrinsic resolution of the resist described here is excellent and capable of printing  $0.18\text{--}0.25\text{-}\mu\text{m}$  features.



*Figure 4-3. Resist profiles for sample using 1% bis(t-butylphenyl) iodonium triflate PAG. The process conditions were the same as for Figure 4-2. The exposures were carried out at 193 nm on a prototype stepper with 0.5 numerical aperture. The scanning electron micrographs illustrate features (a) 0.3, (b) 0.35, (c) 0.4, and (d) 0.5  $\mu\text{m}$ .*



*Figure 4-4. Resist profile for sample whose composition and process conditions were the same as for Figure 4-3, but in this case a chromeless phase-shifting mask was used. The linewidth is  $0.1\ \mu\text{m}$  and the resist thickness  $0.5\ \mu\text{m}$ .*

One drawback to the current formulation is poor etch durability. At present, the plasma etch resistance of the resist is similar to that of PMMA, and efforts are under way to improve it. One method already reported involves incorporation of high C/H-ratio pendant groups such as adamantyl or norbornyl [5],[6]. Once the etch durability is improved, these systems are expected to yield an inexpensive, stable, high-resolution resist capable of providing a manufacturable  $0.20\text{-}\mu\text{m}$  process.

R. R. Kunz

W. D. Hinsberg\*

R. D. Allen\*

G. M. Wallraff\*

## 4.2 DIAMOND FIELD-EMISSION CATHODE TECHNOLOGY

A robust cold cathode would enable the fabrication of flat-panel displays with the color fidelity and viewing characteristics found in existing cathode-ray tubes (CRTs). The primary requirements for such a cathode are that it be resistant to poisoning and operate at very low fields with sufficient current density. We have demonstrated that diamond field emitters can meet these requirements. Exposure to a contaminant dose equivalent to ten years of continuous use had no effect on emission current or voltage. Operation has been achieved for several diamond emitter configurations at fields below  $15\ \text{V}/\mu\text{m}$ .

---

\*Author not at Lincoln Laboratory.

In our first test of a diamond cathode [7], a vertical diode was fabricated in diamond with the junction exposed to vacuum. When forward biased, the electrons traveled from the conduction band in an *n*-type region into the conduction band in a *p*-type region. Some of the electrons near the edge of the device were emitted into the vacuum and were collected by a small anode. The ratio of the emitted current to the diode current was approximately  $10^{-5}$ . These initial experiments indicated that a more efficient emitter would be required for the display application and that an improved experimental apparatus would be needed to measure the emission characteristics of the cathodes.

We have recently completed a major upgrade to the experimental apparatus. The new vacuum system is oil-free and typically operates at a base pressure of  $3 \times 10^{-9}$  Torr. A residual gas analyzer indicates that the primary remaining gases in this new system are water and carbon dioxide. A three-axis manipulator has been installed to allow 1- $\mu\text{m}$  precision in setting the anode-to-cathode spacing and in selecting the location on the sample to test. The anode is a 1-mm-diam molybdenum wire with the end mechanically polished. The distance to the cathode is usually set to 100  $\mu\text{m}$  so that the error in field due to tilt of the anode is held to a few percent. The anode potential is set by a computer-controlled high-voltage power supply. The diamond cathode is mounted on an electrically isolated hot stage. The temperature of the stage is measured using an optically isolated thermocouple gauge. The current extracted from the cathode is measured with an electrometer with a sensitivity of  $10^{-15}$  A. Finally, the capacitance between the anode and the cathode is measured and digitized, which allows an in-situ measurement of the anode-to-cathode distance to within a few percent. The separation distance is used to calculate the electric field at the sample given the (measured) applied potential. As the current and voltage are sampled the capacitance is measured to detect if the electrostatic forces on the sample cause it to move.

This new apparatus was used to measure the electron emission from single-crystal diamond films, in order to provide quantitative information about the emission physics. Boron-doped homoepitaxial diamond was grown on polished single-crystal substrates, and the emission characteristics of the (100) and (110) facets were measured. As seen in Figure 4-5, the (110) surface emits at far lower voltage than the (100) surface. Since this cannot be explained by geometry-induced field enhancement or scaling the emitting area, we conclude that the tests demonstrate the (110) crystal face has a lower work function than the (100) face.

Conductive surfaces with sharp tips can concentrate the electric field in the vicinity of the tip. This raises the surface field at the tip, substantially reducing the potentials required to achieve field emission. Thus, the shape of the emitter can be manipulated to our benefit. Figure 4-6 shows our first attempt to control the geometry of a single-crystal diamond emitter by etching posts into a (100) surface. The measured emission before and after etching the sample is shown in Figure 4-7. There are two factors that account for the enhanced emission. Etching the (100) surface exposes other crystal planes with lower work functions along the sides of the pillars, and field concentration occurs at the edges and corners of the pillars further enhancing emission.

The etched-post sample exhibited emission behavior indicative that a single post was providing most of the current. At high currents ( $> 10$  mA), as the applied field was raised the current would suddenly step lower, suggesting that we had destroyed the emitting post and that a neighboring post was now carrying the current. Subsequent microscopy of the emitting area showed that the area under the

anode was missing posts, whereas the rest of the sample demonstrated a uniform post array. The strong implication is that the entire 15 mA came from a single post. This emission current is a factor of 30 larger than the highest current ever seen from a metal Spindt-type cathode [8]. Under the conservative assumption that the entire top of the post is emitting with an area of  $1 \mu\text{m}^2$ , the calculated current density would be  $1.5 \times 10^6 \text{ A/cm}^2$ .

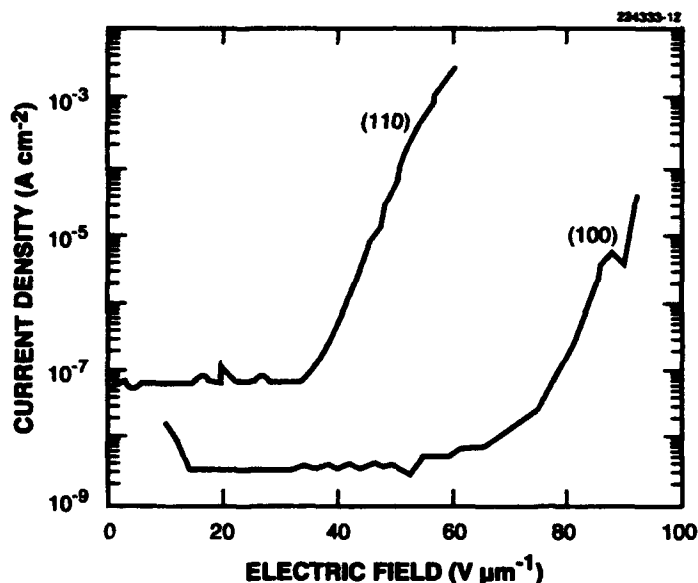
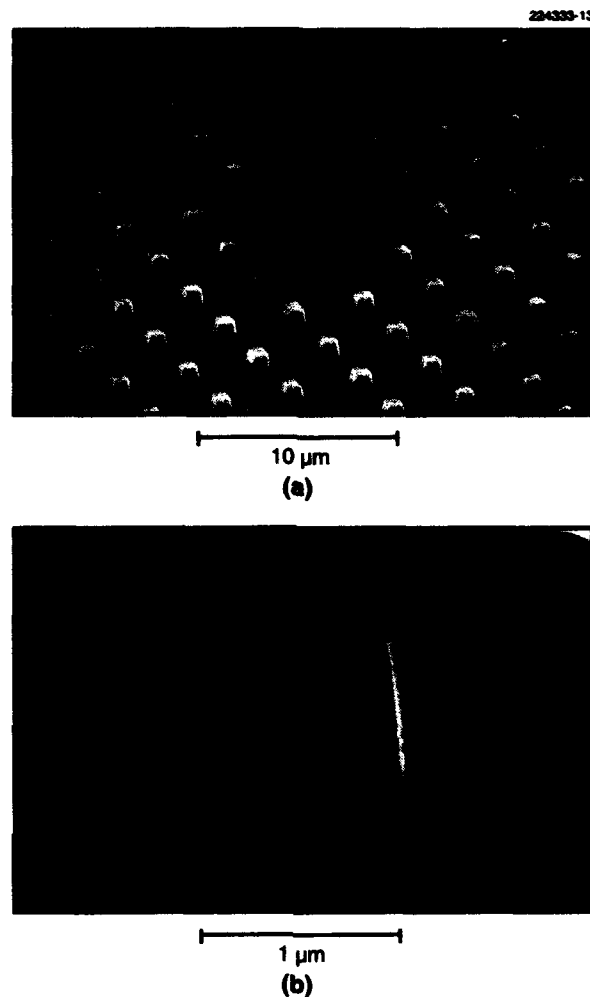


Figure 4-5. Measured emission characteristics of (100)- and (110)-oriented films fabricated by boron-doped homoepitaxy on single-crystal diamond substrates. The current vs voltage characteristic is strongly dependent on the crystal orientation of the substrate.

Diamond has several unique properties which make this current density possible. The current that can be extracted from a local region (a tip) is limited by heating. The thermal conductivity of diamond is  $20 \text{ W cm}^{-1} \text{ K}^{-1}$  at room temperature, compared with  $1.4 \text{ W cm}^{-1} \text{ K}^{-1}$  for the standard molybdenum Spindt emitter. In addition, while molybdenum's resistivity increases with temperature, the resistivity of boron-doped diamond decreases with increasing temperature because the dopant is not fully ionized at room temperature. This mechanism stabilizes the diamond temperature. Finally, diamond will not form a liquid on the emitter tip. If the diamond is pure it will graphitize and sublime at about  $3500^\circ\text{C}$ . Metals, on the other hand, liquefy at high temperature, which lowers the work function. This radically increases the current, causing catastrophic failure.



*Figure 4-6. Scanning electron micrographs of (a) array of posts etched into a (100)-oriented, single-crystal diamond substrate and (b) detail of one such diamond post.*

A series of tests was performed to establish the resistance of diamond field emitters to degradation in performance due to residual vacuum contaminants. This degradation, called poisoning, typically limits the life of thermionic emitters. Many such emitters will not tolerate even exposure to air. Our experiments indicate that diamond emitters tolerate not only air, but cleaning in water and acetone, boiling sulfuric acid, and oxygen plasma. The true test of the stability of the cathode is a lifetime test. By raising the pressure and operating the cathode at high current, two important lifetime limits can be probed. First, the lifetime charge emitted, called the Coulomb limit, can be measured by operating the cathode at a constant current for a period of hours. Second, poisoning due to ion flux or neutrals can be determined. In a Coulomb limit test conducted at 1000 times the normal CRT pressure, both the ion flux and neutral flux are similar to the lifetime display dose, but the testing may be conducted in a matter of hours.

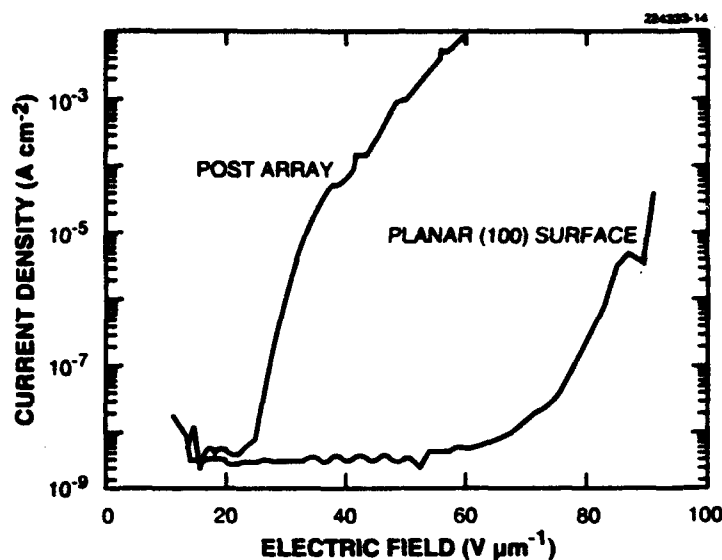


Figure 4-7. Comparison of the emission characteristics of planar, (100)-oriented, single-crystal diamond film and post array etched into the same film.

Significant uncertainty exists regarding the residual gas composition in an operating display. Many common contaminants were used in an attempt to simulate the display environment. Argon, water, nitrogen, oxygen,  $\text{SF}_6$ , and dimethyl ether were tested. Water vapor reduced the emitted current, but subsequent operation recovered the normal current. All other gases had essentially no effect after 1000 s of dc operation at  $10^{-3}$  Torr. (Since CRTs typically operate at pressures below  $10^{-7}$  Torr, measurements at  $10^{-3}$  Torr provide a severe test of the emitter life.) No other emitter of any type used commercially is this robust. Diamond field emitters have demonstrated the critical properties necessary for a cold cathode in a flat-panel display. Future efforts will concentrate on reducing the required potentials and designing inexpensive emitters suitable for mass production.

J. C. Twichell  
M. W. Geis

## REFERENCES

1. R. D. Allen, G. M. Wallraff, W. D. Hinsberg, and L. L. Simpson, *J. Vac. Sci. Technol. B* **9**, 3357 (1991).
2. G. M. Wallraff, R. D. Allen, W. D. Hinsberg, C. G. Wilson, L. L. Simpson, S. E. Webber, and J. L. Sturtevant, *J. Imaging Sci. Technol.* **36**, 468 (1992).
3. W. D. Hinsberg, S. A. MacDonald, N. J. Clecak, and C. D. Snyder, *Proc. SPIE* **1672**, 24 (1992).
4. Acknowledgment is made to F. Zernike and S. Stanton of SVG Lithography Systems, Inc., Wilton, Conn., for their assistance in performing the exposures that produced the results shown in Figures 4-3 and 4-4.
5. Y. Kaimoto, K. Nozaki, S. Takechi, and N. Abe, *Proc. SPIE* **1672**, 66 (1992).
6. M. Endo, K. Hashimoto, K. Yamashita, A. Katsuyama, T. Matsuo, Y. Tani, M. Sasago, and N. Nomura, presented at International Electron Devices Meeting, San Francisco, Calif., 14-18 December 1992.
7. Solid State Research Report, Lincoln Laboratory, MIT, 1991:3, p. 28.
8. C. A. Spindt, C. E. Holland, A. Rosengreen, and I. Brodie, *IEEE Trans. Electron Devices* **38**, 2355 (1991).



## 5. HIGH SPEED ELECTRONICS

### 5.1 PHOTONIC-CRYSTAL PLANAR ANTENNAS

Photonic crystals are structures having a spatially periodic variation of permittivity, with the simplest version, and the type used here, being a high-permittivity dielectric in which air voids are fabricated at the points of a Bravais lattice. Through the process of Bragg scattering from this lattice, the photonic crystal presents a range of frequencies, called the photonic bandgap, in which electromagnetic radiation cannot propagate [1]. This property makes the photonic crystal in many ways the electromagnetic analog of a semiconductor. As such, it is well suited to several applications in electromagnetic signal propagation. One very important application that has recently been demonstrated at Lincoln Laboratory is the photonic-crystal planar antenna. The antenna consists of a coplanar metallic-strip radiator, such as a dipole, mounted on the surface of a photonic crystal and driven at a frequency lying within the photonic bandgap. Experimentally, the antenna has yielded a radiation efficiency from microwave transmission lines into free space above the substrate of nearly 100% [2].

Planar antennas play the important role in microwave and millimeter-wave integrated circuits of radiating signals from transmission lines into free space. When fabricated monolithically from semiconductors, integrated circuits offer superior performance and higher functional density than alternative circuits made by hybrid techniques. However, the relevant semiconductors all have a high permittivity ( $\epsilon > 10$ ), which generally hinders the performance of planar antennas. The large  $\epsilon$  causes a majority of the total output power of the antenna to radiate into the substrate and to be trapped there by total internal reflection [3]. As a result, the radiation efficiency from millimeter-wave planar antennas on homogeneous semiconductor substrates into free space above the substrate is usually less than 10%.

An elegant way to solve this problem is to mount the planar radiator on a three-dimensional photonic crystal, as depicted in Figure 5-1. When driven at a frequency lying within the photonic bandgap, the planar antenna can radiate power into free space above the substrate only, because propagation is forbidden into the full hemisphere on the substrate side. This approach was first tested by mounting a bow-tie antenna on the (111) face of a face-centered-cubic photonic crystal having a bandgap between ~ 13 and 16 GHz. This crystal was manufactured at Bellcore by drilling holes in a synthetic dielectric material having  $\epsilon = 12$  [4]. The antenna patterns were measured at 13.2 GHz using the setup depicted in Figure 5-1.

The experimental antenna patterns in the electric (E) plane are shown in Figure 5-2(a). The radiated power is confined predominantly to the air side of the antenna, as desired. To show the benefit of the photonic-crystal substrate, measurements were also made on an identical bow-tie antenna fabricated on a uniform dielectric substrate having the same permittivity as the solid portion of the photonic crystal. This pattern is shown in Figure 5-2(b), and as expected, very little power is radiated into the air side. The results for the two antennas in the magnetic (H) plane were similar. The bow-tie antenna on the photonic-crystal substrate radiates nearly 100% of the drive power into free space, whereas the antenna on the uniform dielectric radiates the majority of the drive power into the substrate.

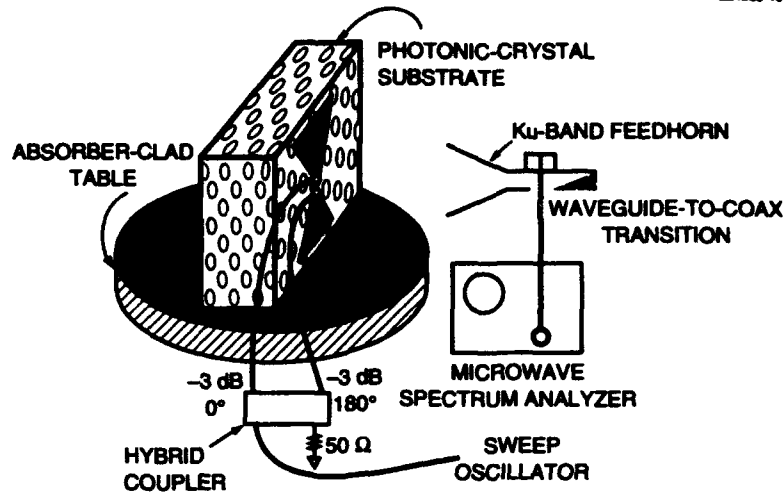


Figure 5-1. Schematic diagram of bow-tie antenna mounted on three-dimensional photonic-crystal substrate. Also shown is the experimental setup used to measure the radiation patterns at 13.2 GHz.

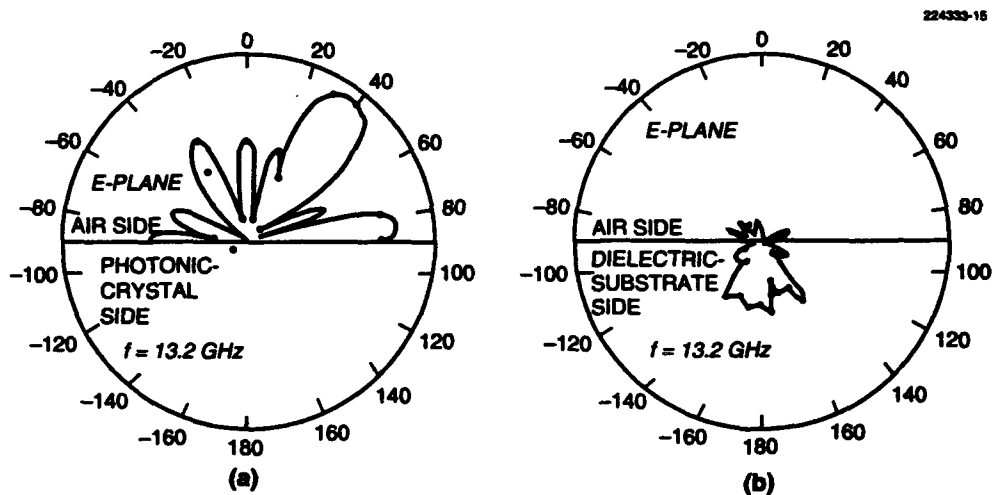


Figure 5-2. (a) Radiation pattern at 13.2 GHz measured over 360° in the E-plane for bow-tie antenna on photonic-crystal substrate (radial scale linear in power). (b) Radiation pattern measured for same bow-tie antenna as in (a) but on uniform-dielectric substrate.

The photonic-crystal planar antenna is particularly attractive for monolithic integrated circuits because it can be fabricated from the same semiconductor materials used to make high-speed electronic devices. The photonic crystal would constitute a small section of the wafer below and around the radiating metallic strips. The strips would be coupled to electronic devices fabricated nearby on homogeneous sections of the wafer. The high efficiency of the planar antenna in this configuration could dramatically improve the performance of active phased arrays, which are presently of great interest in millimeter-wave radar and communications applications.

E. R. Brown  
C. D. Parker

## REFERENCES

1. E. Yablonovitch, *Phys. Rev. Lett.* **58**, 2059 (1987).
2. E. R. Brown, C. D. Parker, and E. Yablonovitch, *Opt. Photon. News* **3**, 37 (1992).
3. D. B. Rutledge, D. P. Neikirk, and D. P. Kasilingam, in *Infrared and Millimeter Waves*, Vol. 10 (Academic, Orlando, 1983), p. 1.
4. E. Yablonovitch, T. J. Gmitter, and K. M. Leung, *Phys. Lett.* **67**, 2295 (1991).

## 6. MICROELECTRONICS

### 6.1 METHOD FOR MEASURING QUANTUM EFFICIENCY OF CCD IMAGERS

One of the critical aspects of a charge-coupled device (CCD) imager is its quantum efficiency. However, compared to other CCD performance measures, such as dark current and charge-transfer inefficiency, quantum efficiency is more difficult to determine and is subject to more uncertainties and sources of error. We describe here a new measurement technique that offers several advantages in reducing errors over the methods currently employed. This technique has been compared with a standard approach on a back-illuminated device, and the two methods give good agreement.

One of the simplest techniques for measuring quantum efficiency is to illuminate the CCD with a monochromatic light source of known flux while operating the device as a simple photodiode. All the CCD gates are biased to the same dc voltage level, and the photocurrent is measured at the reset drain, which is the terminal at which the output charge from the device usually appears. This method has the virtues of allowing direct measurement of the photocurrent and permitting the use of chopped light sources with synchronous detection, which is advantageous for rejecting drift (e.g., from dark current) and stray light and for enabling measurement at low signal-to-noise ratios. However, questions can be raised as to whether the biasing conditions are such that photoelectrons can flow to the reset drain in time periods shorter than the chopping period. This issue is of particular concern with the current generation of large imagers which have areas in excess of  $10\text{ cm}^2$ . Even with a dc light source, this measurement technique does not permit the device to be operated with bias conditions and charge levels in the CCD wells that are representative of normal operation.

A technique that overcomes these objections is to operate the device in the normal imaging mode and to digitally record the output video. The photoelectron count in each frame is obtained by first subtracting a reference frame previously recorded with the light off, converting each pixel voltage to charge, and then summing the charge from all the illuminated pixels. This method therefore requires a careful measurement of the charge-to-voltage conversion factor, or responsivity, of the output circuit over the range of anticipated signal levels. Unlike the photodiode method, it precludes using chopped-light/synchronous detection with its attendant advantages.

We describe here a method, which we shall term the clocked photodiode method, that incorporates the best features and avoids the disadvantages of the techniques just described. The CCD is illuminated with a chopped light source of period  $T_L$ , while both the parallel and serial registers of the device are clocked with period  $T_c$ . Figure 6-1(a) depicts a device with a  $3 \times 3$  array of uniformly illuminated pixels, Figure 6-1(b) illustrates the square-wave-modulated photon flux incident on the device, and Figure 6-1(c) shows the amplitude  $Q(t)$  of the output charge packets as a function of time in response to the modulated photon flux. The chopped light source produces an output charge that is roughly trapezoidal but can be assumed to be a square wave for sufficiently low chopping frequencies or small illuminated areas. Under this assumption, the CCD output charge can be measured with a lock-in amplifier synchronized to chopped light. It is also possible to measure the photocurrent on the substrate leads of the device, in which

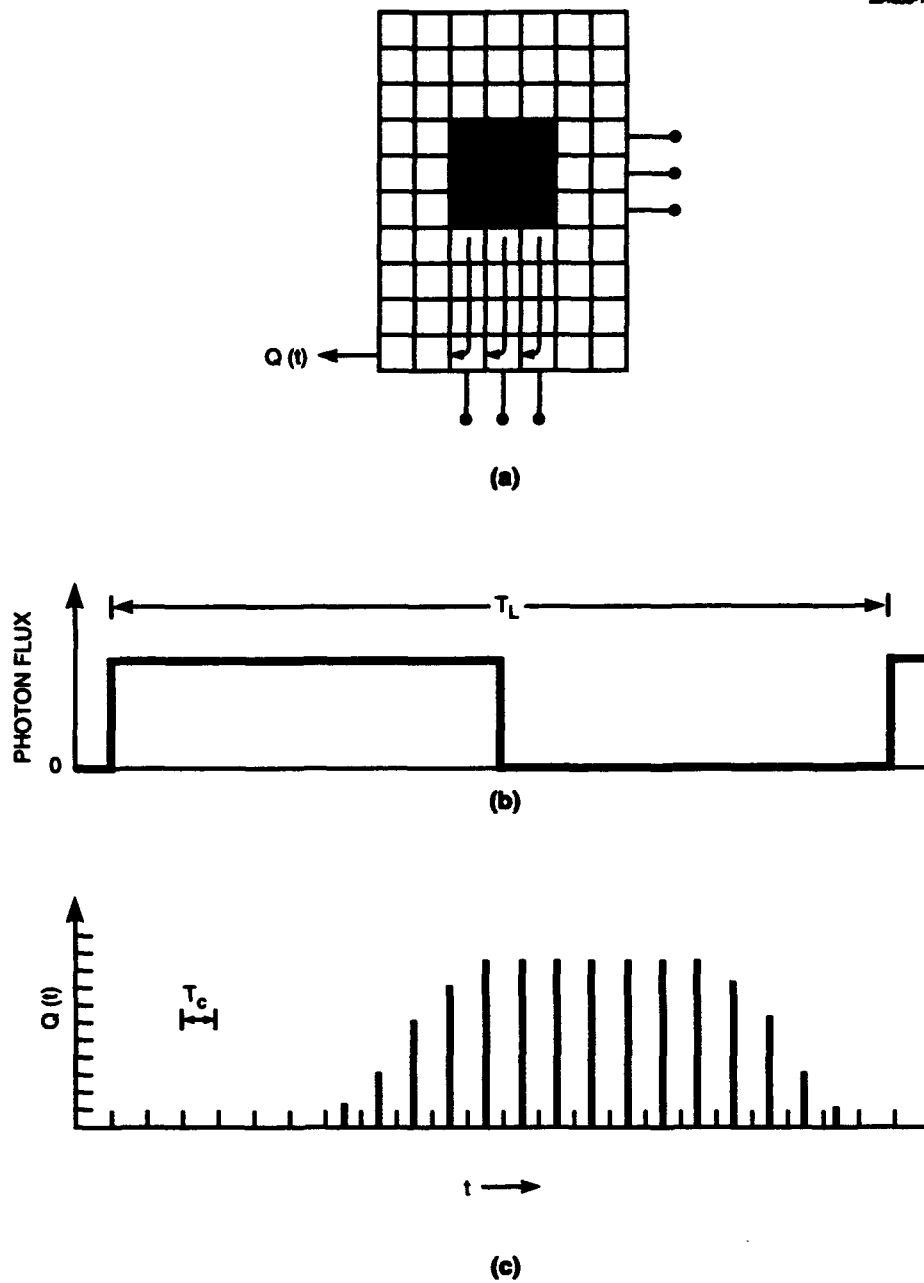


Figure 6-1. (a) Charge-coupled device with  $3 \times 3$  array of uniformly illuminated pixels. (b) Square-wave-modulated photon flux incident on the device. (c) Amplitude  $Q(t)$  of output charge packets as function of time in response to the modulated photon flux.

case the current would be a square wave irrespective of the clocking scheme. However, it is usual in CCD test systems and cameras for the substrate leads to be tightly wired to system grounds, for reasons pertaining to noise, and therefore not as readily accessible as the reset drain.

Figure 6-2 illustrates the experimental configuration for this method. The monochrometer output is monitored by a reference detector during the measurement so that any drift in the incident radiation flux can be taken into account. The system is first calibrated by replacing the CCD with a photodiode that has in turn been calibrated to a primary standard by NIST. Reflecting optics are used to maintain a constant illuminated area on the device independent of wavelength. The CCD charge is clocked to the reset drain of the output circuit, and the resulting photocurrent is then converted to a voltage in a transimpedance amplifier. The technique therefore retains the advantage of the regular photodiode method by performing a direct measurement of the photocurrent without the need for responsivity measurements. This simplifies the quantum efficiency measurement and avoids the complications of occasional nonlinearities in the responsivity at high charge levels. Also, we believe that the responsivity measurement itself is more prone to errors than the photocurrent-voltage conversion in the transimpedance amplifier.

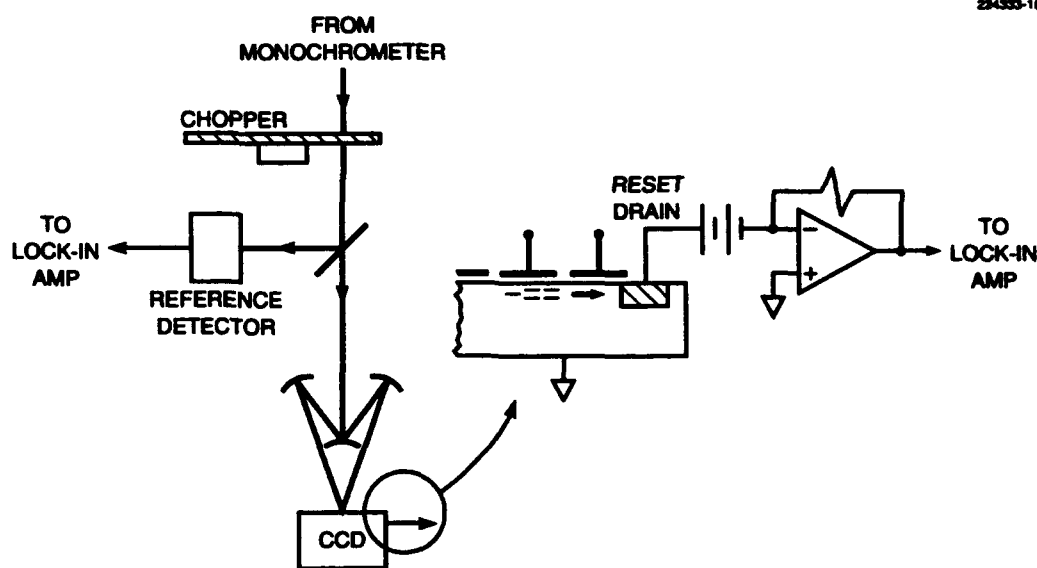


Figure 6-2. Experimental configuration for quantum efficiency measurement technique.

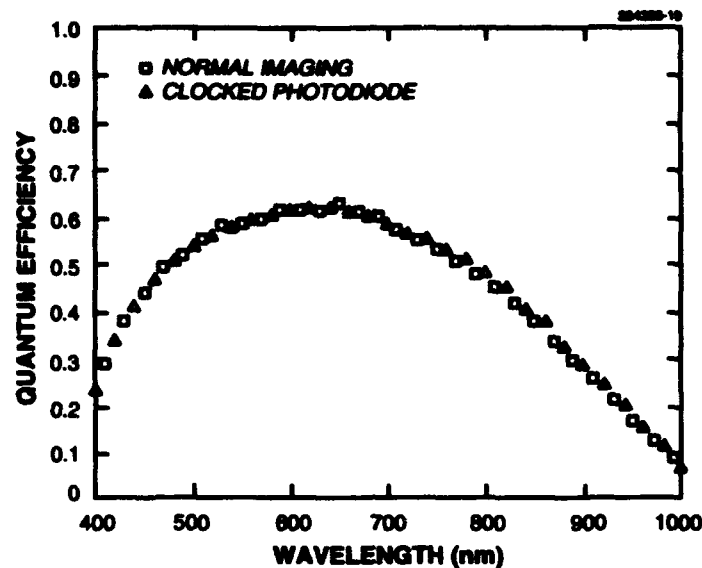


Figure 6-3. Comparison of quantum efficiency measured using normal imaging and clocked photodiode techniques.

In a comparison of the clocked photodiode method with the normal imaging method described earlier, we used a back-illuminated  $420 \times 420$ -pixel frame-transfer imager. This device is approximately  $10 \mu\text{m}$  thick and has a shallow  $p^+$  layer created by ion implantation and activated by a pulsed laser anneal [1]. The quantum efficiency was measured over the wavelength range 400–1000 nm, and the device was at a temperature of  $-50^\circ\text{C}$ . The illuminated area of the device was a circular region about 100 pixels in diameter in the imaging area. For the clocked photodiode method the clocking frequency was 400 kHz, resulting in a photocurrent rise time at the CCD output of about 0.25 ms. Since the chopping period was 25 ms, the CCD signal could be safely assumed to be a square wave. The results from the two methods are shown in Figure 6-3, and the agreement is excellent.

B. E. Burke

H. R. Clark, Jr.

## REFERENCES

1. B. E. Burke, J. A. Gregory, R. W. Mountain, J. C. M. Huang, M. J. Cooper, and V. S. Dolat, *Proc. SPIE* 1693, 86 (1992).

## 7. ANALOG DEVICE TECHNOLOGY

### 7.1 CYLINDRICAL MAGNETRON DEPOSITION OF HIGH-QUALITY HIGH-TEMPERATURE SUPERCONDUCTIVE THIN FILMS

The discovery of high-temperature superconductivity in copper oxide compounds [1] has led to a worldwide effort to deposit thin films of these new materials [2]. Magnetron sputtering was one of the first methods that was tried [3], since it had been successfully used for the deposition of many complex oxides [4]. However, when a variety of conventional sputtering methods (dc, RF, magnetron) were investigated, most workers noted that the composition of the sputtered films differed appreciably from that of the target and the films had low superconducting transition temperature  $T_c$  or were not superconductors. The problem was traced to the presence of negative oxygen ions [5], which after being created at the target surface and accelerated by the electric field into the dark space region adjacent to the target, struck the substrate and preferentially sputtered copper from the film, thus interfering with film growth.

Soon after this problem was identified, three solutions were proposed to circumvent it [6]–[8]. One used an off-axis geometry, in which the substrate was placed perpendicular to the target to avoid substrate bombardment [6]. A second used a cylindrical geometry similar to the one shown in Figure 7-1 to accomplish the same effect [7]. The third used very high sputtering pressures (100 times higher than in conventional techniques) to thermalize the fast negative ions by collisions in the gas phase before they reached the substrate [8]. All three methods eventually produced very high quality films. However, off-axis and high-pressure sputtering are very inefficient and quite slow, with deposition rates  $< 50$  nm/h. Furthermore, the most widely used of these methods, off-axis sputtering, usually produced films with rough surfaces that became progressively rougher with increasing film thickness, eventually limiting the maximum film thickness to  $\sim 300$  nm, thinner than the optimum value of 600–800 nm for microwave applications. For the cylindrical magnetron geometry, about half of the material sputtered from the target is deposited onto the substrate, so fairly high rates ( $\sim 1$   $\mu\text{m/h}$ ) can be easily achieved. Despite this apparent advantage, however, its widespread utilization has lagged considerably behind the other methods, mainly because of a lack of commercially available sources capable of large-area deposition and a less developed target technology.

Here, we describe a 4-in.-diam cylindrical magnetron capable of depositing uniform, smooth films with superior microwave properties. Figure 7-1 shows the cross section of our design. The target is a hollow cylinder of  $\text{YBa}_2\text{Cu}_3\text{O}_{7-\delta}$  with an i.d. of 9.5 cm, o.d. of 10.4 cm, and a height of 4.1 cm. The magnetic structure for the cylindrical magnetron, which was designed using a commercially available software program [9], consists of two main parts. The magnets behind the targets and the pole pieces with U-shaped cross section define the main magnetic field responsible for trapping the electrons near the cathode. The maximum parallel field at the target surface was designed to be 160 G, using a criterion adapted from the one developed for planar targets by Goree and Sheridan [10]. Lower magnetic fields are less effective in trapping electrons, while higher fields would only confine electrons to a narrower band, thereby decreasing target utilization without any further increase in trapping efficiency. All the other pole pieces and magnets are part of an auxiliary structure that directs electrons scattered out of the main trapping ring toward the anode and away from the substrate. Electrons directed toward the substrate,



usually a very good insulator, tend to charge it negatively, which attracts the positive ions abundant in the plasma. The resultant ion bombardment can produce preferential sputtering of copper and interfere with film growth, an effect similar to the negative ion bombardment that the cylindrical structure is supposed to avoid. Measurements with electrical probes in a 2-in.-diam magnetron prototype had shown that stray magnetic fields crossing the substrate produced a considerable amount of ion bombardment. The bombardment was much more intense near the walls of the target. This led to nonuniform film properties and limited the area of good films to  $< 1 \text{ cm}^2$ . It is the same effect that apparently is also present in the only commercially available cylindrical magnetron source.

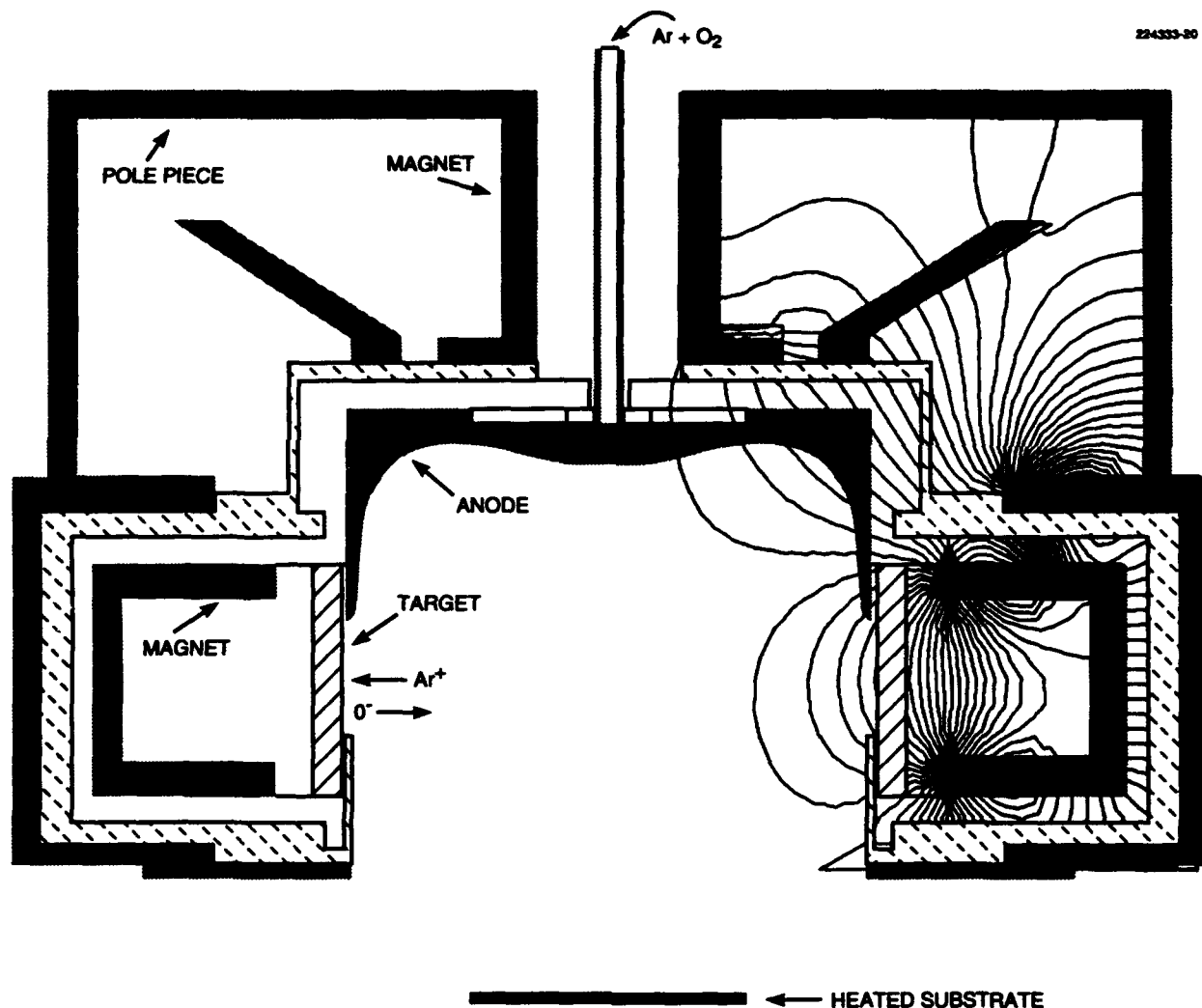


Figure 7-1. Cross section of cylindrical magnetron. The magnetic field lines superposed on half of the figure were calculated using commercially available software [9].

**TABLE 7-1**  
**Parameters for Cylindrical Magnetron Film Deposition\***

Cathode current	2.0 A
Cathode voltage	160 V
Anode voltage	5.0 V
Anode current	2.0 A
O <sub>2</sub> partial pressure	90 mT
Total pressure (Ar + O <sub>2</sub> )	180 mT
*The films with the best RF properties were deposited in a mixture of H <sub>2</sub> :O <sub>2</sub> :Ar of 1:8:9. The total gas pressure was 180 mT. All films were deposited onto LaAlO <sub>3</sub> (001) substrates.	

Our best films to date have been deposited with the parameters shown in Table 7-1. Films with  $T_c$  ( $R = 0$ ) = 90 K have been deposited uniformly over 2-in. wafers, the largest substrate that can be heated in our current system. The surface of these films can be very smooth with no visible features up to 20 000 magnification in a scanning electron microscope for samples as thick as 800 nm.

A typical x-ray diffraction pattern is shown in Figure 7-2. Only peaks (00 $\ell$ ) are observed, showing that the film is oriented with the c-axis perpendicular to the substrate. In higher-resolution scans, the splitting between the CuK $_{\alpha 1}$  and CuK $_{\alpha 2}$  x-ray lines for all peaks above (004) is observable, attesting to the very high degree of orientation of the films.

The surface resistance as a function of peak RF magnetic field at the film surface is shown in Figure 7-3. In the same figure we also plot representative values for off-axis-sputtered films and for films deposited by high-pressure sputtering [11]. The high-current surface resistance for the cylindrical magnetron films is the lowest ever reported for films deposited by any method. This extends the applications of superconductors to high-power communication devices, an area with potential for wide commercial applications and where superconductivity can have a significant advantage over competing technologies.

A. C. Anderson      D. E. Oates  
R. L. Slattery      L. S. Yu-Jahnes

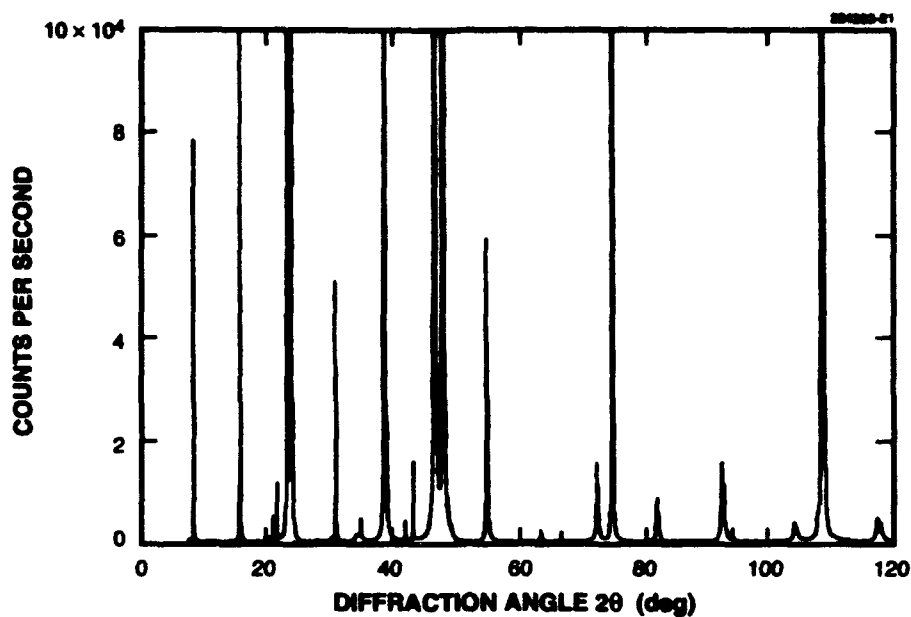


Figure 7-2.  $2\theta$  diffraction pattern of 800-nm  $\text{YB}_2\text{C}_3\text{O}_{7-\delta}$  thin film.

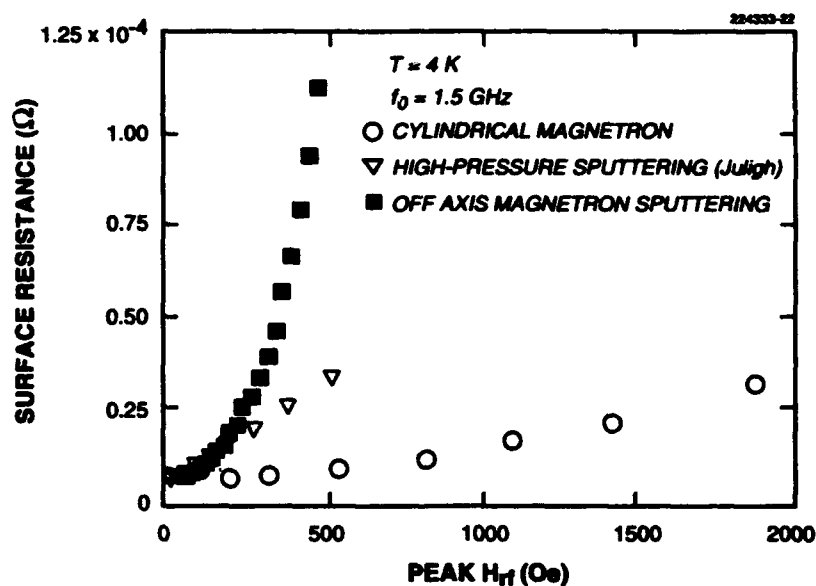


Figure 7-3. Surface resistance as function of peak RF magnetic field produced by RF currents circulating in center conductor of stripline resonator.

## 7.2 TUNNEL-DIODE SHIFT REGISTER USING TUNNEL-DIODE COUPLING

Resonant-tunneling diodes (RTDs), because of their very high ratio of current density to specific capacitance, are capable of switching extremely rapidly. For example, oscillators have been made that operate above 700 GHz [12]. Building complex logic circuits from two-terminal devices, however, poses a greater challenge. For one thing, the devices have to switch over a wide voltage range and cannot be restricted to the range where they respond at their highest speed. For another, the same terminal has to be used as both the input and the output, making isolation a problem. We report here on a new approach for realizing a digital shift register with RTDs that, based on simulations, is expected to reach speeds in the 50-GHz range. The circuit is simple, requires RTDs and Schottky diodes only, provides relatively wide operating margins, and is capable of fan-in and fan-out.

Any digital circuit requires basic elements that have two discrete states. Figure 7-4 shows such an element using an RTD. The current source  $I_{inj}$  represents the combination of input drive currents and output load currents to which the circuit is subjected at its common input/output (IO) node. Both  $I_{inj}$  and  $V_{dd}$  may be time varying.

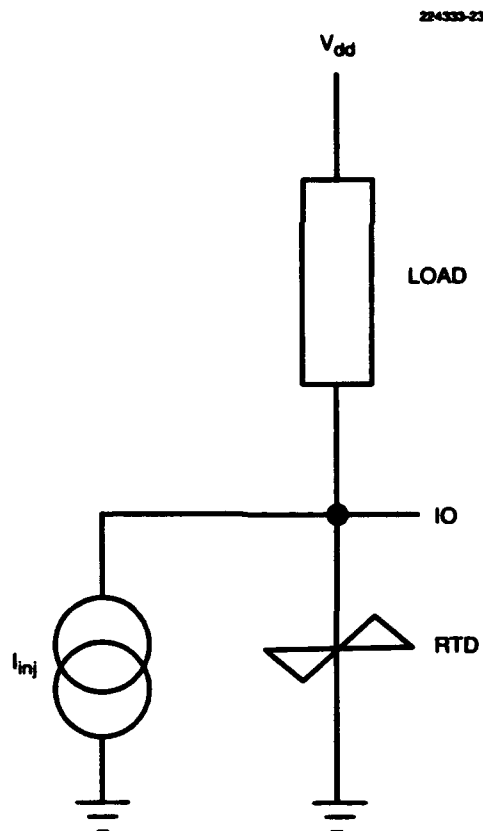


Figure 7-4. Basic resonant-tunneling diode (RTD) latch circuit.

A load-line graphical analysis makes it easy to visualize the operation of the circuits discussed here. Figure 7-5(a) shows a composite current-voltage (I-V) plot for the RTD and for the load device, which in this case is a second, slightly lower current RTD. The I-V plot for the load device has its origin at  $(V_{dd}, I_{inj})$  and is reflected about the  $V = V_{dd}$  line. Points where the two I-V curves cross are equilibrium

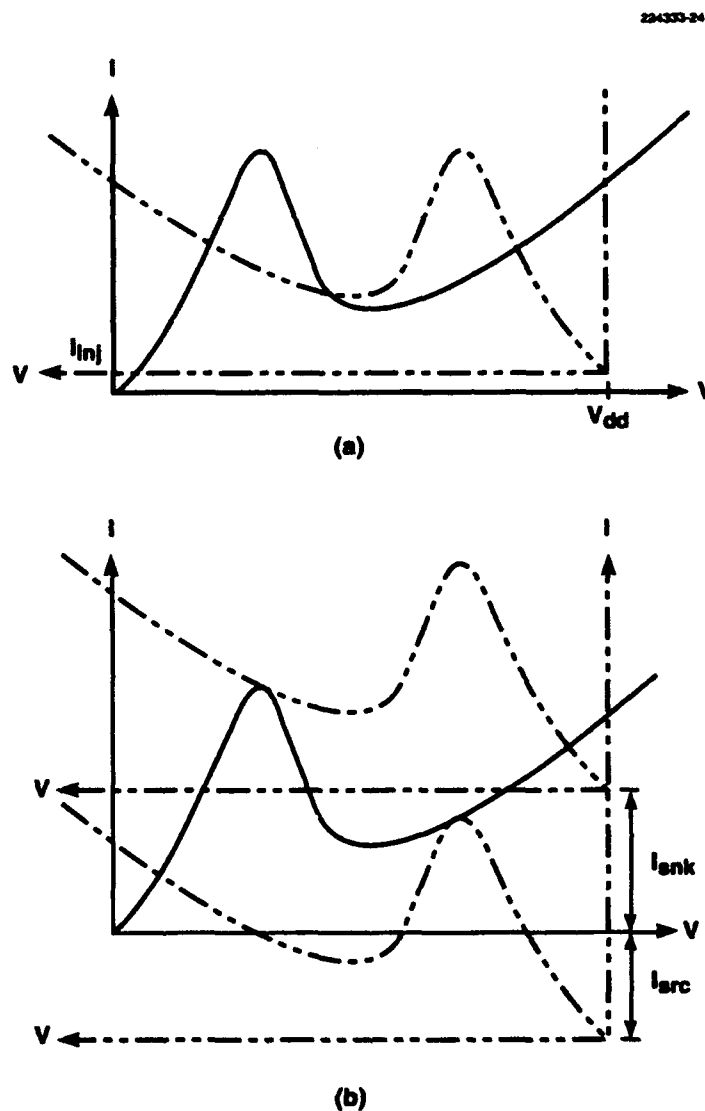


Figure 7-5. Load-line graphical technique for analyzing behavior of RTD latch. The current-voltage (I-V) curves are solid and the load lines dashed. (a) Curves for a value of  $I_{inj}$  for which there are three equilibrium states, two stable and one unstable. (b) Curves for the extreme values of  $I_{inj}$  beyond which only one stable equilibrium state remains. In (b) the upper dashed curve shows the maximum current  $I_{sink}$  that the latch can sink while in its low state before it switches to the high state, and the lower dashed curve shows the maximum current  $I_{src}$  that the latch can source while in its high state.

states. For appropriate values of  $V_{dd}$  and  $I_{inj}$ , as in Figure 7-5(a), there are three such states. The middle state is unstable, while the high and low states are stable and can represent digital logic values. For other values of  $V_{dd}$  and  $I_{inj}$  one of the stable states disappears. Figure 7-5(b) presents curves for the extreme values of  $I_{inj}$  beyond which one of the stable states disappears. The upper curve shows the maximum current  $I_{snk}$  that the latch can sink while in its low state before it switches to the high state. The lower curve shows the maximum current  $I_{src}$  that the latch can source while in its high state.

A shift register is made by connecting a series of latches in such a way that a logic state can be transferred from one latch to the next under the control of clock signals. Our first shift register design employed a static  $V_{dd}$  supply and induced switching by coupling currents into the latch—from the previous stage and from clocks—that exceeded  $I_{src}$  and  $I_{snk}$ . The coupling circuits used diodes and capacitors, and several clamp circuits involving additional diodes and power supplies were required to maintain the coupling capacitors in the required bias range. This design provided the required functionality, but it was complex, operated over only a limited range of frequencies for a given choice of capacitor values, and had tight operating margins.

The second design, which is described here, operates the latch in a different way—by applying the clock signal to the  $V_{dd}$  node. The basic circuit shown in Figure 7-6, but using Esaki tunnel diodes, was first proposed in 1962 by Aleksander and Scarr [13]. Two clock phases are applied to alternate latches, and the latches are coupled by rectifying diodes. The clocks are normally at a voltage level that results in two stable states, and they are pulsed alternately to a lower voltage at which there is only one stable state. With a load RTD that is slightly smaller in area (and hence peak current) than the active RTD, the latch will go into the low state when no current is injected through the coupling diode, as is the case when the previous latch is in the low state. On the other hand, if current is injected through the diode, as is the case when the previous latch is in the high state, then the latch will go into the high state. In this way, the digital data will be propagated through the shift register. The operation is illustrated by the sequence of I-V plots in Figure 7-7.

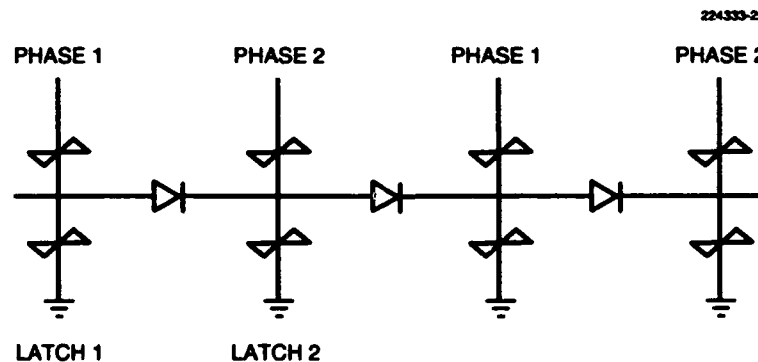


Figure 7-6. Schematic of tunnel-diode shift register proposed by Aleksander and Scarr [13].

Several factors determine the design margins for this circuit. There is the obvious dynamic constraint that latch 1, when in its high state, must be able to inject enough current through the coupling diode to cause latch 2 to switch into its high state. Additionally, there are static constraints that apply when both clocks are high and when latches 1 and 2 are in their high and low states, respectively: the current flow through the coupling element must be less than  $I_{src}$  so that latch 1 will not drop to its low state, and it must be less than  $I_{snk}$  so that latch 2 will not flip to its high state.

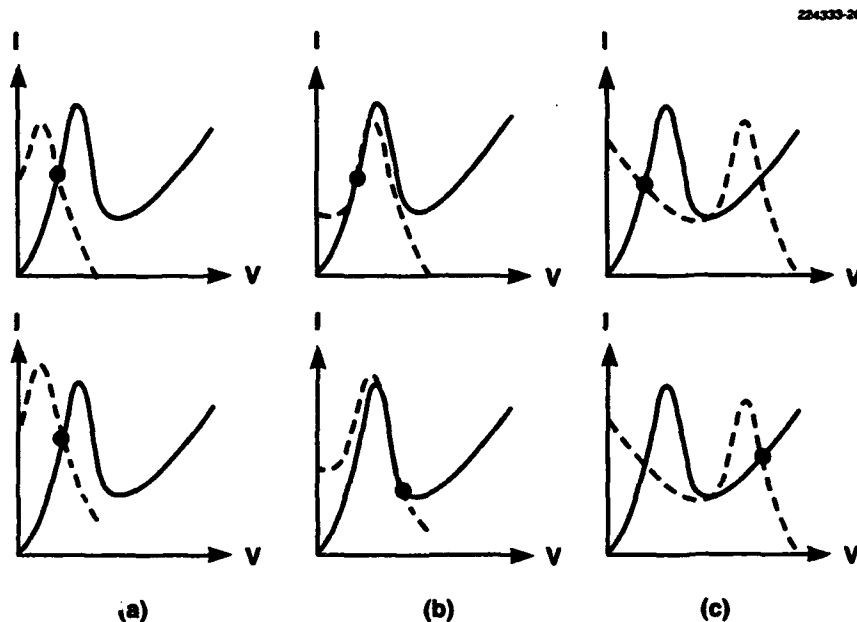


Figure 7-7. Sequence of I-V curves (solid) with load lines (dashed). The sequence shows how the state of the latch evolves as the clock voltage, having been pulsed low, returns to its normal high voltage. The upper curves are for the case of no current injected into the latch, and the lower curves for current injected into the latch. The clock voltages are low, in the critical interval, and high for (a), (b), and (c), respectively.

From the I-V curves in Figure 7-7 one can see that there is a critical voltage interval within the positive transition of the clock during which the final state of the latch is determined. That critical interval occurs around the point when the current peaks of the two RTDs overlap, that is, when the clock voltage is twice the voltage  $V_{pk}$  at which the RTD current reaches its peak. If the injected current during the critical interval exceeds a threshold value  $I_{crit}$ , then the latch will switch to the high state. Injection of current significantly outside the critical interval is not required for the transition to occur. Clearly,  $I_{crit}$  must be less than both  $I_{src}$  and  $I_{sink}$  for the circuit to work. In our designs,  $I_{crit}$  is typically about 20% of  $I_{pk}$ . Since  $I_{src}$  is typically more than 60% of  $I_{pk}$ , a fan-out of two can be supported comfortably.

A conventional diode is not the ideal interstage coupling element, because its current continues to increase—and increase rapidly—as the voltage drop across it increases. If the diode is designed to provide at least  $I_{\text{crit}}$  over the critical interval of the clock cycle, then it will inject far greater current while the clock voltage is at its lowest value. At the worst, that current level may exceed  $I_{\text{src}}$  of the latch in the previous stage and cause the shift register to lose information. At best, it will reduce margins, severely limiting the fan-out capability of the circuit.

The ideal coupling element would provide current mainly during the critical part of the clock transition. Our new circuit accomplishes this by adding an RTD in series with the coupling diode. Consider the following slightly simplified analysis based on some typical values. Assume that the latch is made from RTDs with  $V_{\text{pk}} = 0.8$  V and that the clock voltage is chosen to give latch-stable states of 0.5 and 2.2 V. The critical interval occurs around a clock voltage of 1.6 V ( $2V_{\text{pk}}$ ), at which point the latch IO node is at 0.8 V ( $V_{\text{pk}}$ ). The drop across the coupling element is then  $2.2 \text{ V} - 0.8 \text{ V} = 1.4 \text{ V}$ . This is exactly where the peak current flow will occur for the series combination of a Schottky diode (forward drop 0.6 V) and an RTD ( $V_{\text{pk}} = 0.8$  V).

A prototype of this circuit was constructed using discrete RTDs, and its operating principles were verified. Figure 7-8 shows oscilloscope traces of the input signal and the voltages at the first two latch IO nodes during the experiment. High-speed operation was not possible because of parasitic capacitances

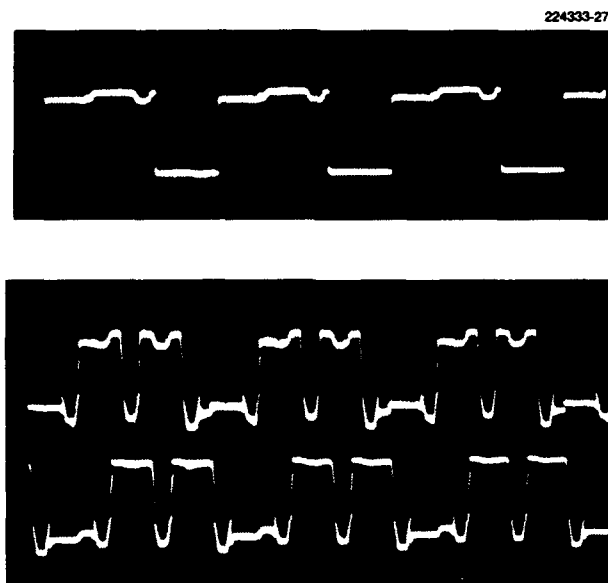
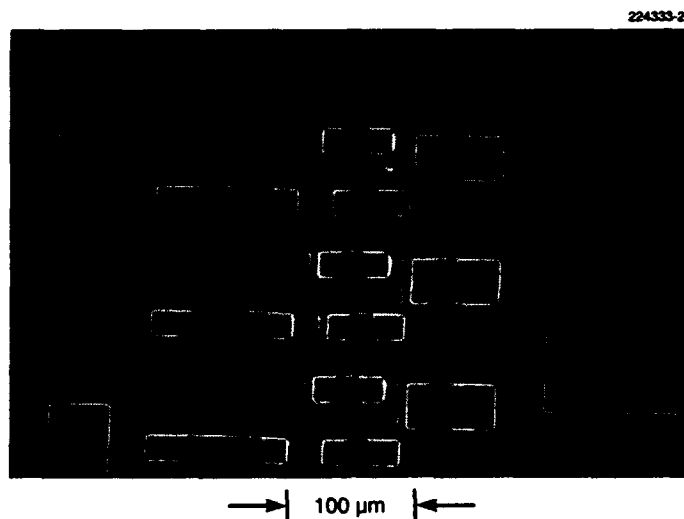


Figure 7-8. Oscilloscope traces during operation of prototype shift register using discrete components. The upper trace shows the input signal applied to the first latch, and the bottom two traces show the voltages at the input/output nodes of the first two latches. The timing of the two clock phases can be seen from the lowest output levels of the latch signals.





*Figure 7-9. Scanning electron micrograph of first monolithic implementation of RTD-coupled shift register. The two vertical bus bars on the left are the two clock phases. The large bus bar on the right is ground. Pairs of RTDs share each well. In the wells on the left, the large RTD is the load device, and the small one the Schottky-contacted coupling device. The large RTDs in the wells on the right are the active devices for the two latches that constitute one stage of the shift register.*

and inductances. We have now designed and fabricated a monolithic version of the RTD shift register. A scanning electron micrograph of a circuit on the first wafer is shown in Figure 7-9. The Schottky diodes for the coupling circuit are fabricated integrally with the RTD itself by using a rectifying contact to the top of the coupling RTD. Defects in the processing unfortunately prevented us from operating circuits from this first fabrication run. A second run is now under way.

J. P. Sage	C. L. Chen
R. H. Mathews	W. D. Goodhue
T. C. L. G. Sollner	

## REFERENCES

1. J. G. Bednorz and K. A. Müller, *Z. Phys. B* **64**, 189 (1986).
2. See, for example, articles in *Materials Research Society Symp. Proc.*, Vol. 99 (Materials Research Society, Pittsburgh, 1988).
3. M. Kawasaki, S. Nagata, Y. Sato, M. Funabashi, T. Hasegawa, K. Kishio, K. Kitazawa, K. Fueki, and H. Koinuma, *Jpn. J. Appl. Phys.* **26**, L736 (1987).
4. J. L. Vossen and J. J. Cuomo, in *Thin Film Processes*, J. L. Vossen and W. Kern, eds. (Academic, New York, 1978), p. 11.
5. S. M. Rossnagel and J. J. Cuomo, *AIP Conf. Proc. on Thin Film Processing and Characterization of High-Temperature Superconductors*, Vol. 165 (American Institute of Physics, New York, 1988), p. 106.
6. R. L. Sandstrom, W. J. Gallagher, T. R. Dinger, and R. H. Koch, *Appl. Phys. Lett.* **53**, 444 (1988).
7. H. C. Li, G. Linger, F. Ratzel, R. Smithy, and J. Geerk, *Appl. Phys. Lett.* **52**, 1098 (1988).
8. X. X. Xi, H. Geerk, G. Linker, Q. Li, and O. Meyer, *Appl. Phys. Lett.* **54**, 2367 (1989).
9. EMP, Field Precision, Albuquerque, N.M.
10. J. Goree and T. E. Sheridan, *Appl. Phys. Lett.* **59**, 1052 (1991).
11. U. Poppe, N. Klein, U. Dähne, H. Soltner, C. L. Jia, B. Kabius, K. Urban, A. Lubig, K. Schmidt, S. Hensen, S. Orbach, G. Müller, and H. Piel, *J. Appl. Phys.* **71**, 5572 (1992).
12. E. R. Brown, J. R. Söderström, C. D. Parker, L. J. Mahoney, K. M. Molvar, and T. C. McGill, *Appl. Phys. Lett.* **58**, 2291 (1991).
13. I. Aleksander and R. W. A. Scarr, *J. Br. IRE* **23**, 177 (1962).

## REPORT DOCUMENTATION PAGE

Form Approved  
OMB No. 0704-0188

\*Public reporting burden for this collection of information is estimated to average 1 hour per response, including the time for reviewing instructions, searching existing data sources, gathering and maintaining the data needed, reviewing and revising the content of information, and sending the collected information. Send comments regarding this burden estimate or any other aspect of this collection of information, including suggestions for reducing this burden, to Washington Headquarters Services, Directorate for Information Operations and Reports, 1215 Jefferson Davis Highway, Suite 1204, Arlington, VA 22202-4302, and to the Office of Management and Budget, Paperwork Reduction Project (0704-0188), Washington, DC 20503.

[illegible]